Investigating the Strangeness of Neutron Stars

Shazeab Ayub

Master of Science

University of York

Physics

January 2022

Abstract

A comprehensive understanding of the strong nuclear force is a primary goal of nuclear physics. One step towards a complete understanding is uncovering the dynamics of interactions involving hyperons (strange baryons). While the nucleon-nucleon (NN) interaction has been studied extensively, the nature of the hyperon-nucleon (YN) interaction is largely a mystery. Understanding hyperon interaction could also help paint a better picture of neutron stars by confronting the "hyperon" puzzle".

This work analyses data collected by the g13 experiment, which ran at the Thomas Jefferson National Accelerator Facility, with the key objective of studying the interactions of a Σ^- hyperon, specifically within the $\gamma d \rightarrow K^+\Sigma^-$ reaction. This was done by studying the final state interactions of the reaction of interest, namely, by extracting the beam spin asymmetry (Σ). Σ was extracted using the previously established maximum likelihood technique. The results of the analysis indicate towards Σ^- rescattering events dominating the reaction of interest. The two-fold binning method used isolated kinematic regions within E_γ and $\cos\theta^{c.m.}_{K^+}$ and found that within the range 1.3 GeV < E_γ < 1.9GeV, the Σ rescattering mechanism was especially dominant.

Contents

Declaration

I declare that this thesis is a presentation of original work and I am the sole author. This work has not previously been presented for an award at this, or any other, University. All sources are acknowledged as References.

1 Introduction & Background

1.1 A brief history of the atomic model

The standard model encompasses all four fundamental forces and all known elementary particles (the complete list of known particles is much more vast). During the 20^{th} century a great many particles were discovered and a classification chart was devised to categorise them. Particles are firstly split into hadrons and leptons, the difference being that hadronic particles interact through the strong force whereas leptons do not. Hadrons are made up of the most elementary particles, quarks, which leads to a further categorisation within the hadronic classification; baryons and mesons. Baryons are made up of three quarks as opposed to a two quark pairing in mesons. Despite the current understanding of particle physics being quite vast, it is a relatively new field of physics with most of the major advancements and discoveries coming within the last 150 years.

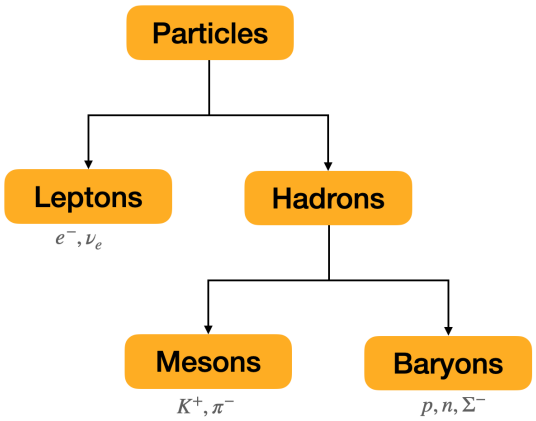

Figure 1: A schematic showing a loose classification of particles. A short list of examples is also listed under each group of particles.

In 1897, the electron became the first fundamental particle to be discovered [1]. After studying cathode rays at the Cavendish Laboratory, J.J. Thompson came to the conclusion that the rays were made up of a new type of particle, the electron, which were the same regardless of which metal was used as the cathode. He also calculated the charge to mass ratio of the electron to be more than 1000 times smaller than that of the hydrogen atom. The hydrogen atom was not thought to have any constituent parts, which led Thompson to a new atomic model which would become to be known as the plum pudding model [2]. The plum pudding model was described as negatively charged electrons (analogous to the plums) embedded within a sea of positive charge (analogous to the pudding).

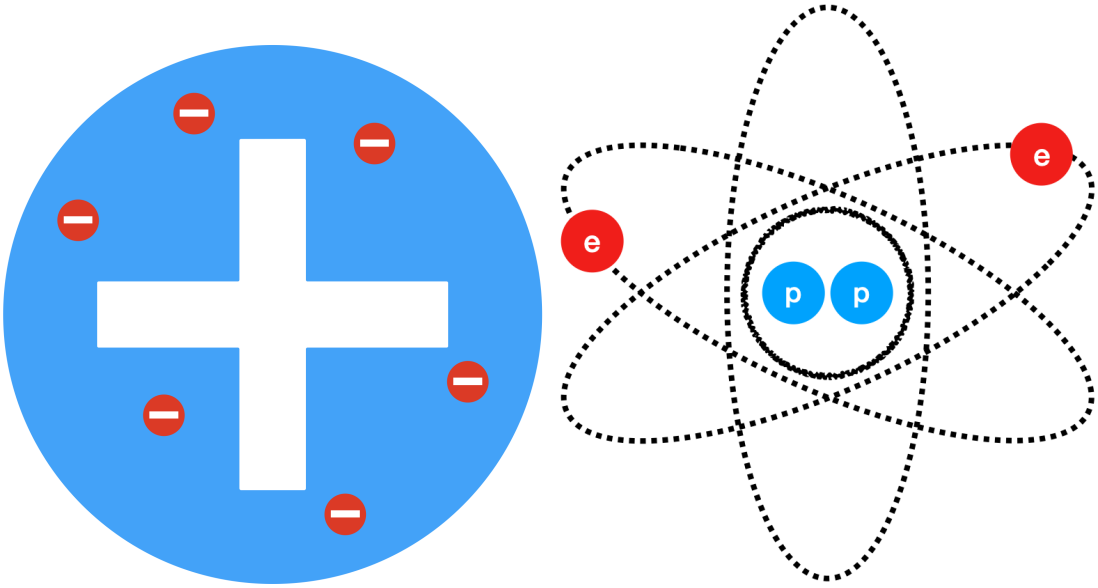

Figure 2: J.J. Thompson's plum pudding model on the left. Rutherford's planetary model on the right.

The next major development came in 1911, when Ernest Rutherford (a student of J.J.Thompson) proposed the planetary atomic model. Rutherford arrived at this model after his now famous gold foil experiment [3]. During the experiment, Rutherford and his students (Hans Geiger and Ernest Marsden) struck a thin sheet of gold foil with a beam of α particles. They noticed that most of the particles did not interfere and travelled straight through the gold foil, however, a small amount of particles were deflected or scattered. This was not consistent with the plum pudding model and so Rutherford concluded that the atom was mostly made up of empty space and that negatively charged electrons orbit a positively charged nucleus. Niels Bohr later modified the planetary model, unifying it with quantum theory. Bohr proposed that electrons have distinct energy levels and in turn, distinct orbital shells [4].

Today it is well established that an atom is made of protons, electrons and neutrons. The neutron was not discovered up until 1932, when James Chadwick repeated an experiment, previously completed by Frederic and Irene Joliot-Curie [5], studying the radiation emitted by beryllium after aiming it at a hydrocarbon target. They concluded that the radiation must carry no charge and they also found that the radiation was heavy enough to knock protons out of the hydrocarbon target. Chadwick deduced that this new radiation must be a new elementary particle. He called it the neutron [6]. Quickly after the discovery of the neutron, Werner Heisenberg suggested a proton-neutron atomic nucleus model [7] more akin to the model seen in textbooks today.

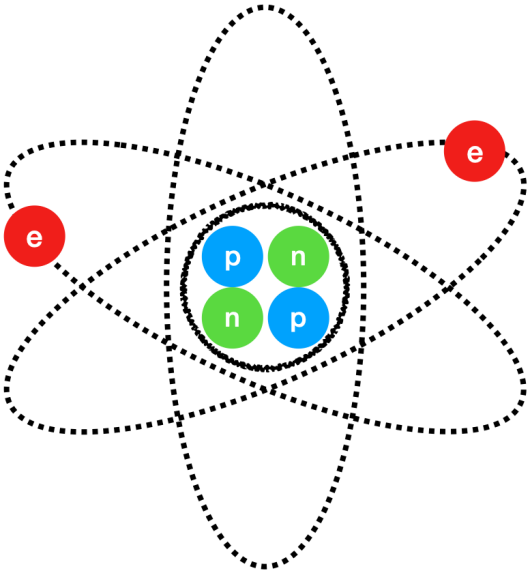

Figure 3: A atomic model more consistent with today's view. It should be noted, however, that the atomic model has been further developed to incorporate quantum mechanics.

1.2 The strong interaction and strangeness

Today, the strong force is known to be the strongest of the four fundamental forces, but its discovery did not come until the 1930's. In 1933, one of the major problems in physics was related to the interaction between nucleons. Specifically, the interaction between two nucleons was identical regardless of whether they were protons or neutrons. Eugene Wigner came up with a solution by predicting the existence of the strong nuclear force [8]. Wigner posited that the force holding atomic nuclei together was not the electromagnetic force and instead the strong force binds nucleons to one another and is the same regardless of the type of nucleon. This fitted nicely with the concept of isospin. Isospin was a a theory proposed a year earlier [9] that claimed that protons and neutrons could both be classified as nucleons, with the difference between the two being their orientations in isospin. Wigner proposed that isospin was a conserved property in strong interactions. The years following saw a number of new particle discoveries.

After the prediction of the strong force, Hideki Yukawa predicted a new type of particle [10]. Yukawa suggested that there must be particles exchanging the strong nuclear force within the atomic nucleus. 12 years after Yukawa's prediction, physicists discovered a particle matching his description [11]. This new particle, named pion, became the first meson to be discovered. Consistent with Yukawa's prediction, mesons are known to be the carriers of the strong force. In the same year, another meson, the kaon, was also discovered [12]. While studying high energy cosmic rays, physicists observed pairs of particles seemingly appearing from an unknown neutral particle. Over the next few years, more attempts to find these particles were made and a second

particle was also discovered (the Λ baryon). One of the more puzzling aspects of these new particles was the "strange" behaviour they exhibited when decaying. Both the kaon and Λ particles were produced almost instantly but had a much slower decay time. In 1953, Murray Gell-Mann explained this by introducing a new property which he labelled strangeness. To solve the decay time problem, strangeness must be conserved in strong interactions but not conserved in weak interactions. The observed kaon and Λ particles must have been created via the strong force and decay via the much slower weak force.

Eleven years later, Gell-Mann postulated new elementary particles which were the constituent parts of already known particles [13], which he named quarks. Each quark would have a fractional value for charge, which defied the conventional wisdom of the time. He also postulated that quarks were confined within subatomic particles and could not be observed individually. Furthermore, Gell-Mann put forward that there were three types of quarks; up, down and strange. All hadrons are differing combinations of these three quarks, for example, the proton is made of two up and one down quarks. The strange quark is the only one with non-zero strangeness, therefore they must be present in the kaon and Λ particles. In the years since, the existence of quarks has been experimentally proven and the model expanded to a total of six quarks; up, down, strange, charm, top and bottom.

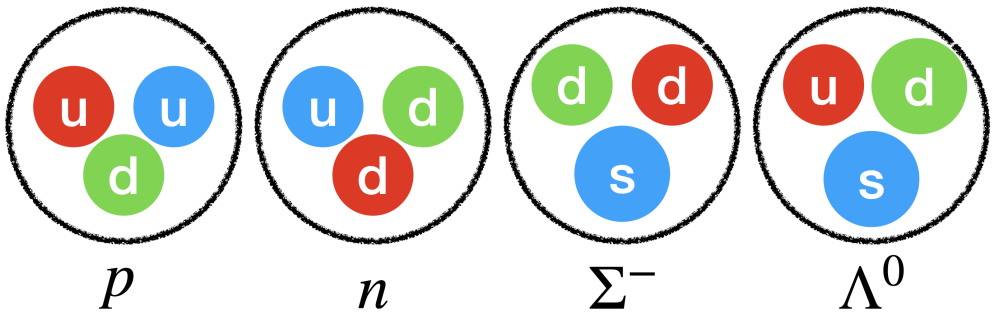

Figure 4: Diagram showing the quark content of a proton, neutron and sigma baryon.

The problem with the quark model was brought forward quickly after its formation. Pauli's exclusion principle states that no two particles can occupy the same quantum state. This meant that particles should not be allowed to contain any more than one quark. This problem was overcome by introducing a new property of quarks named colour charge [14]. Each quark can either be red, blue or green. A baryon containing 3 quarks would have to hold one of each colour, together creating a neutral colour charge. Years later, Gell-Mann built upon the colour charge theory by introducing gluons. He described gluons as the force mediators between quarks, which also carried a colour charge. The theory of the strong force between gluons and quarks, known as quantum chromodynamics (QCD), has become an integral part of the standard model.

1.3 Hyperons

Hyperons are a further subsection of baryons. Baryons containing one or more strange quarks, and not containing top, bottom or charm quarks, are classified as hyperons. Hyperons are naturally heavier than nucleons, since the strange quark is heavier than the up and down variants. Seeing as hyperons are a class of hadrons, they all interact through the strong force. The Λ particle became the first hyperon to be discovered in 1950 [15]. More persuasive proof, in the form of various experiments, followed in the next few years. Since then, hyperons have only been studied through a number of bubble chamber experiments conducted in the mid 1960's. In contrast to the well-defined nucleon-nucleon interaction, little is known about interactions involving hyperons. Unfortunately, hyperons decay very quickly through the weak force in usual terrestrial conditions. Subsequently, to understand hyperon interactions, the final state interactions of hyperon decay products must be used to reconstruct the associated hyperon.

There are four types of hyperon; Λ, Σ, Ξ and Ω hyperons. Each hyperon is made up of three quarks, at least one of which is a strange quark. The other two remaining quarks can be any combination of up, down and strange. For example, the Σ^- hyperon (studied in the following analysis) is made of two down and one strange quark (as seen in Fig. 4).

1.3.1 Hyperon interactions

Compared to the nucleon-nucleon (NN), the hyperon-nucleon (YN) interaction is not well understood. Fig. 5 compares the cross-sectional data collected for the NN and YN interactions. The cross-section encompasses the dynamics of a reaction by describing the probability that particles will react in a certain way. It is immediately apparent, from the number of data points, that the YN is far more restricted than the NN interaction. Additionally, the statistical uncertainties of the YN interaction are far bigger than those of the NN interaction, meaning that the NN data is much more precise.

Cross-sectional data is hard to acquire and polarisation observables can be used instead to obtain a cleaner insight (it must be noted that cross-sectional data and data obtained through polarisation observables are complimentary to each other. Both sets of data together provide a more comprehensive view of an interaction). In the two-step process utilised and described in this analysis, polarisation observables allow the disentanglement of signal from background. This means that results of the analysis can be tighter constrained to satisfy the specific objectives of the analysis. In this work, the polarisation observable extracted was the beam spin asymmetry, which is described in further detail in Sec. 3.7.

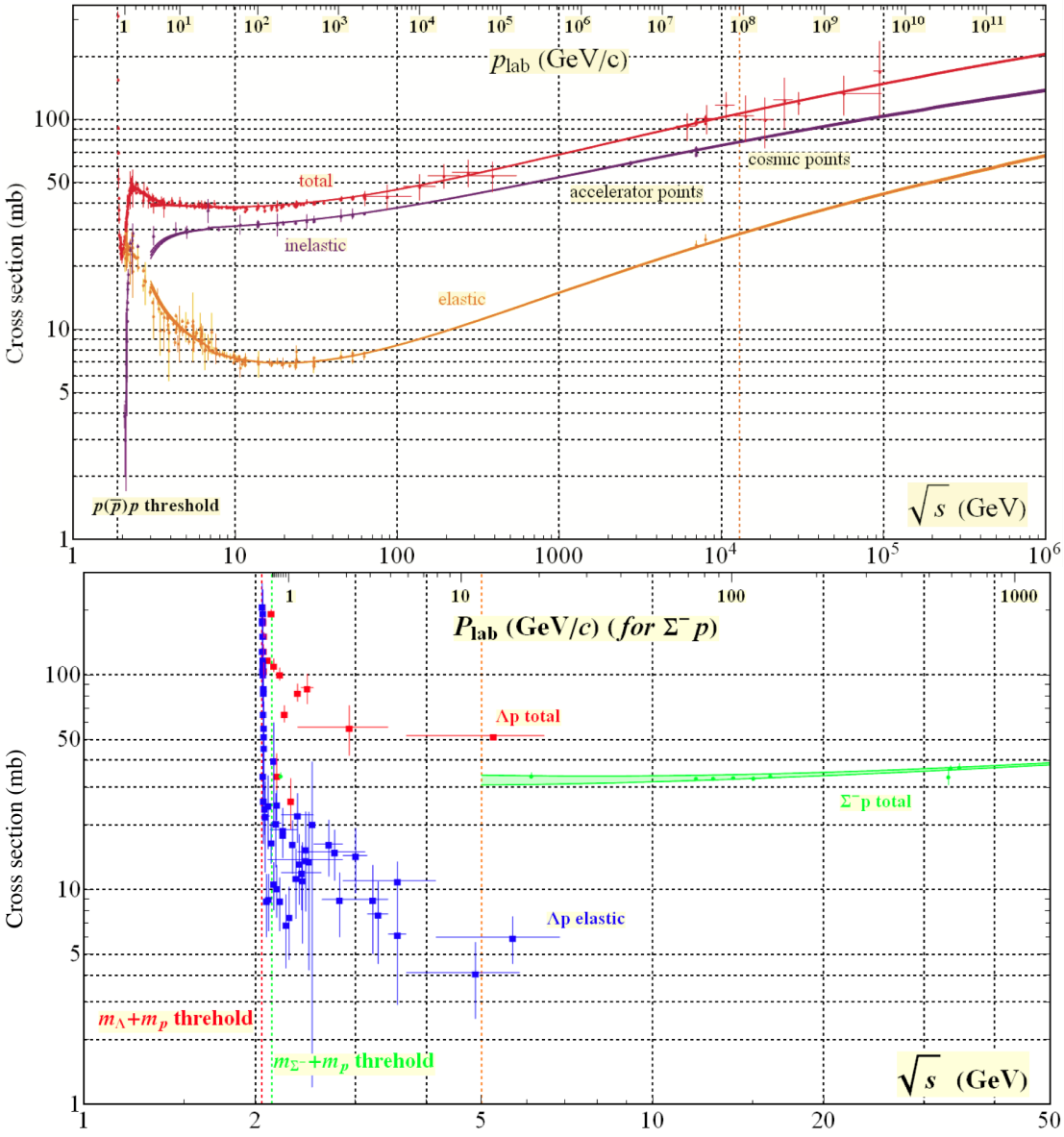

Figure 5: Upper Panel: Current data on the $pp \to pp$ process. Lower panel: Current data on the $\Lambda p, \Sigma p$ processes [16].

A more thorough understanding of hyperon interactions would equate to a deeper understanding of the strong interaction, as well as a more complete neutron star model (more detail in Sec. 1.4).

1.4 Neutron Stars

Neutron stars are some of the most extreme objects in the universe. Neutron stars are the remnants of stars larger than $10M_{\odot}$, after they go supernova. With masses of around $1.4M_{\odot}$ and radii of the order 10km [17] they are some of the most dense objects known today (densities of order $10^{15} g/cm^3$). Neutron stars can also rotate at very high speeds (the fastest spinning neutron star to be found has a frequency of 716 Hz [18]). These properties are just some of the reasons why neutron stars are some of the more interesting objects in the universe.

In 1932, James Chadwick discovered the neutron (as discussed in Sec. 1.1). Shortly after, Baade and Zwicky predicted the existence of dense neutron stars [19] as remnants of supernova explosions. At the time, Wien's law, which relates the temperature of a black body emitter to the wavelength of the emitted radiation, was used to calculate the wavelength of emission for the previously proposed neutron stars. The wavelength was found to be in the x-ray region of the electromagnetic spectrum. Unfortunately, for astronomers of the time, x-rays from space cannot reach Earth's surface and it would be another 30 years before observations from space were possible. In 1967, Jocelyn Bell observed a pulsating signal in the sky. Initially astronomers postulated that the pulsation was due to problems with the equipment, however, this was quickly ruled out. Instead, the origin of this source was determined to be a rapidly rotating neutron star, now called pulsars. Since then, the number of known neutron stars has grown but there are still questions left to be answered.

A neutron star can be described using its equation of state. The relationship between thermodynamic properties such as density and pressure, as well as others, is described through an equation of state. A neutron star can be split into distinct sections (outer crust, inner crust, outer core and inner core) throughout which the equation of state is dynamic. While the equation of state has been calculated within reasonable accuracy, not enough is known about the composition of the inner portions to build a complete neutron star model. Current research in the field aims at finding the composition of the inner segments and consequently a complete neutron star equation of state.

1.4.1 Hyperons in neutron stars

One of the more challenging questions is aimed at the composition of neutron stars. At a minimum, a neutron star must contain protons, neutrons and electrons with more exotic particles believed to be introduced at higher densities. While there are many possibilities regarding the make-up of neutron star cores, hyperons are believed to be present (first predicted by Ambartsumyan and Saakyan in 1960 [20]). The extreme conditions within a neutron star create a vastly different domain, one in which hyperons are stable and their formation is energetically unavoidable. As the density increases within a neutron star, the chemical potentials of protons, neutrons and electrons can increase enough to allow decay into heavier particles. For example the Σ^- hyperon can be created by the $e^- n \rightarrow \Sigma^- \nu_e$ process provided that the chemical potentials (μ) satisfy the condition $\mu_{\Sigma^-} = \mu_{e^-} + \mu_n$ [21]. These conditions begin to be fulfilled at densities of around 2-3ρ_0 (where ρ_0 is the nuclear saturation density) [22].

The introduction of hyperons does however effect the intrinsic properties of neutron stars, which presents problems with hyperonic neutron star models. The "hyperon puzzle" is the name given to a problem relating to the difference between observations and theoretical models of hyperonic neutron stars.

The presence of hyperons produces new degrees of freedom within a neutron star, in turn relieving the degeneracy pressure. This drop in pressure equates to a softening of the equation of state and a lowering of the maximum mass of a hyperonic neutron star. This clashes with current observations. Pulsars J1614-2230 and J0348+0432 were discovered in 2006 and 2007 respectively [23][24], and were calculated to have masses in the region of $2M_{\odot}$. These are masses that cannot be accommodated for by current hyperonic star models. Fig. 6 shows the effect that hyperonic presence has on the maximum mass of a neutron star.

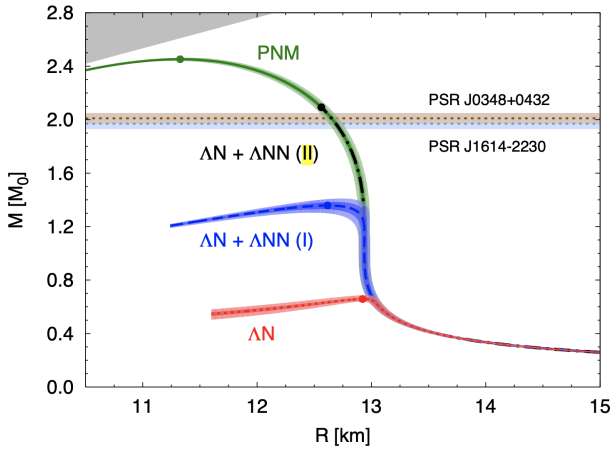

Figure 6: A plot showing how the maximum mass of a neutron star can be affected by it's composition. The green line shows the maximum mass of a neutron star composed of pure nucleonic matter. The red line describes a hyperonic model where only the hyperon-nucleon interaction is accounted for. The blue and black lines describe hyperonic star models that include hyperon-nucleon and hyperon three-body forces. The masses of pulsars J1614-2230 and J0348+0432 are also shown on the plot [21].

The hyperon puzzle describes the mismatch of the hyperonic star model and current observations. As discussed previously, the formation and presence of hyperons within neutron stars is energetically unavoidable, therefore a solution to the hyperon puzzle must be found. To raise the maximum mass of hyperonic stars, a more accurate equation of state must be established. This can only be done by firstly studying hyperon interactions which could contribute to a stiffening of the equation of state. To stiffen the equation of state, a repulsive force between hyperons must be proven. This repulsion can potentially be found between hyperon-nucleon (YN), hyperon-hyperon (YY) or hyperonic three-body (YYY) interactions. Current models suggest that YN, YY and YYY interactions are all needed for the theoretical models to agree with observations. Before a full comprehension of YYY interactions, two-body hyperon interactions must first be studied. Fur-

thermore, to reach an understanding of YY interactions, the hyperon-nucleon interaction must first become better defined.

2 Experimental Setup

2.1 Thomas Jefferson National Accelerator Facility

The data for this analysis was collected using the CLAS detector at the Thomas Jefferson National Accelerator Facility, or more commonly known as JLab. Jlab is located in the U.S. state of Virginia and it accommodates the Continuous Electron Beam Accelerator Facility (CEBAF). While the g13 experiment was being run, CEBAF was able to produce an electron beam with energies up to 6 GeV (it has since been upgraded and is now capable of producing electron beams up to 12 GeV). Fig. 7 shows a simple schematic of CEBAF.

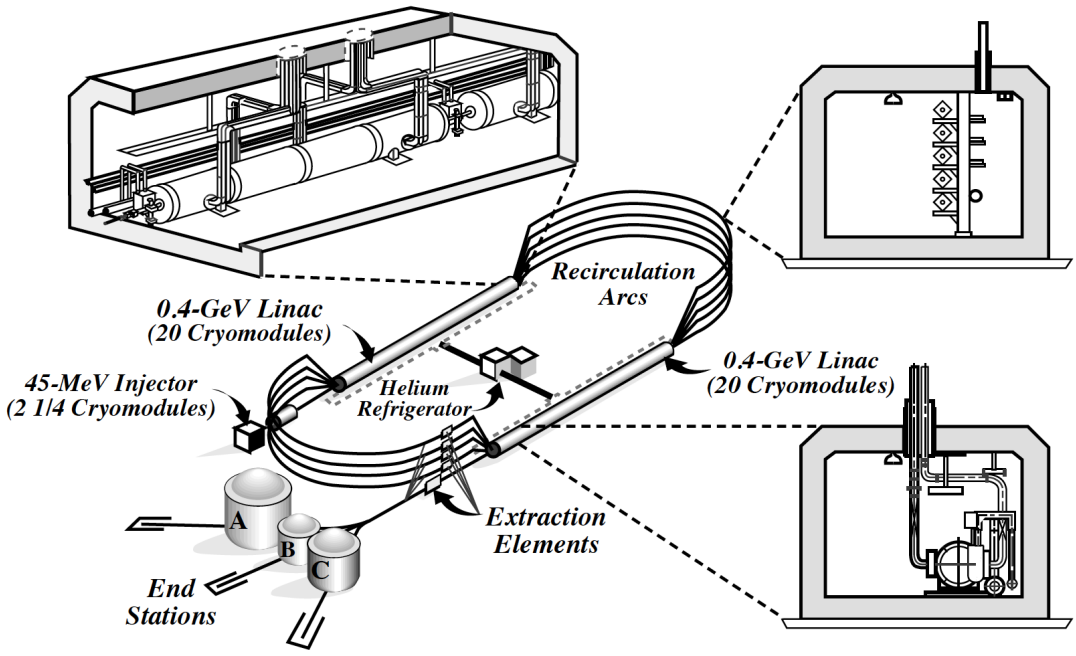

Figure 7: A diagram showing the layout of CEBAF [25].

The electron energy was varied using straight line accelerators (LINACs). Each time the beam passed through the LINACs, it gained 600 MeV. By recirculating the beam up to 5 times, an energy of 6 GeV could be reached. Recirculating the beam fewer times allows a lower energy electron beam. After the required energy was built up, the beam could be delivered to three end stations corresponding to the experimental halls A, B and C.

2.2 The g13 experiment

The g13 experiment ran from October 2006 to June 2007. It used eight different electron beam energies, ranging from 3.3 GeV to 5.16 GeV, producing six different coherent edge positions (the coherent edge is described in Sec. 2.2.1). The g13 experiment was split into two parts. The first used circularly polarised beams (g13a) and the other used linearly polarised photon beams (g13b).

2.2.1 Linearly polarised photons

This study analysed data collected using linearly polarised photon beams collected during the g13b experiment. Linearly polarised photon beams were produced by using a diamond radiator [26] mounted on a goniometer. This was done by altering the orientation of the diamond radiator, held by the goniometer, to a specific angle. This technique produces coherent photons which have sharp rises and drop offs within the photon energy spectra. These can be seen very clearly in the enhancement plot shown in Fig. 8. The orientation of the plane of photon polarisation was alternated on an almost run-by-run basis, between the beam polarisation being parallel to the ground (PARA) and perpendicular (PERP).

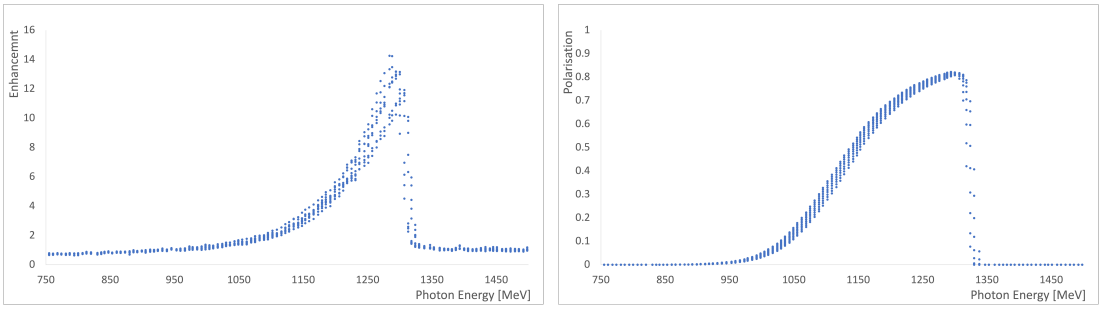

Figure 8: Left: A example of the enhancement distribution. Right: How the degree of polarisation is affected by the coherent edge.

The sharp drop-off points shown in Fig. 8 are referred to as the coherent edge. CLAS collaborators have previously established that photons with energies close to the coherent edge have a lower uncertainty in the degree of polarisation [27][28][29]. Photons within the coherent edge peak have an upper estimate of 8% uncertainty in the degree of polarisation. Sec. 3.4 describes a cut applied to remove events produced by photons with higher associated uncertainties. The panel on the right of Fig. 8 shows photon energy as a function of the degree of polarisation. This information is encapsulated within lookup tables which are used during the analysis (described in Sec. 3.4).

2.2.2 The reaction of interest

The objective of the g13 experiment was to photoproduce kaons using polarised photons on a liquid deuterium target. The event of interest for this analysis was $\gamma d \rightarrow K^+\Sigma^-$. As discussed in Sec. 1.3, in terrestrial conditions, hyperons are very unstable. As a result, the Σ^- hyperon decays too quickly to be observed directly, although before its decay Σ^- can interact with a spectator proton. The decay products ($\pi^- n$) of Σ^- can be detected by CLAS. This leads to the final state $\gamma d \rightarrow K^+\Sigma^-(p) \rightarrow K^+\pi^- n$.

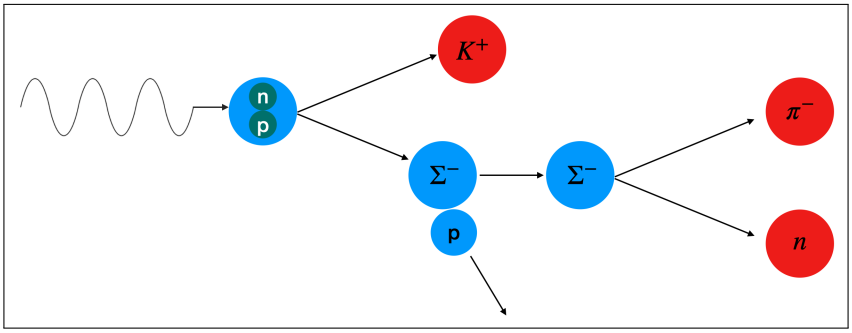

Figure 9: A simplified diagram of the reaction of interest. Before its decay the Σ^- can interact with a spectator proton which is not detected by CLAS. The final state particle that were detected by CLAS are shown in red.

The analysis described throughout Sec. 3 aims to isolate the events of interest using various cuts on the g13b data before attempting to study the extent of any interactions undergone by the Σ^- baryon, as well as the other product particles from the reaction of interest.

2.3 The CLAS Detector

The CEBAF Large Acceptance Spectrometer (CLAS) was housed in Hall B at JLab. The CLAS detector used a number of component parts together to produce exceptionally high quality experimental data, giving access to final state interactions and their kinematical dependencies. A detailed description of the CLAS detector can be found in Ref. [25].

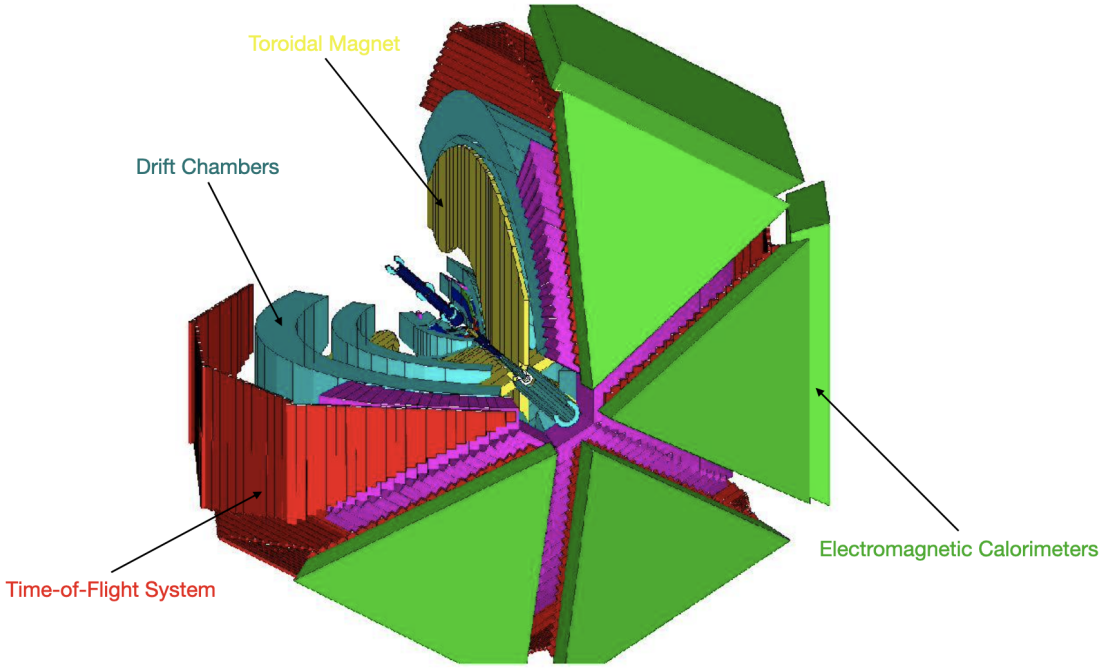

Figure 10: A labelled diagram of the CLAS detector [30].

2.3.1 Tagger

In the timeline of the reaction, the tagger is situated after the diamond radiator and before the deutron target. The electrons used to produce coherent photons from the diamond radiator are detected by the tagger and used to determine the energy of photons incident on the reaction target as well as identifying which photon initiated the reaction. This is done using a magnet in unison with a hodoscope. The magnet redirects electrons from the radiator towards the hodoscope and allows the produced photons to travel onward to the deutron target. The hodoscope is made up of two separate rows of scintillators. The first row consists of 384 scintillator paddles, referred to as E-counters, and the second row contains 61 scintillators, referred to as T-counters. The E-counter which detects the deflected electron corresponds to the energy of the electron and can be used to determine the energy of the photon produced by the detected electron. The T-counters gather timing information and "tag" the photon produced by the electron. A more detailed description of the tagger is given in Ref. [31]

2.3.2 Start Counter

After the photon hits the deutron target, the charged particles produced by the reaction are firstly met by the start counter. The start counter is made of 24 scintillator paddles joined with photo-

multiplier tubes, which are used to match the product particles of the reaction with the photon determined to have produced it (found by the tagger). The scintillators are split into six sections and are spread around the target. The scintillators detect charged particles produced by the reaction. As suggested by its name, the start counter estimates the start time of a reaction. A more detailed description of the start counter can be found in Ref. [32].

2.3.3 Drift Chambers

The drift chambers are used to determine the momentum of the product particles. The drift chambers consist of field wires running around a sense wire in the centre, creating hexagonal patterns. By keeping the field wires at negative potentials and the sense wires at a positive potential, a potential difference is created over the drift chambers. The drift chambers are filled with gas which is ionised by incoming particles. A torus magnet, comprised of six superconducting coils, creates a toroidal magnetic field over the drift chambers which curves the path of charged particles. The drift chambers are detectors that allow the determination of the radius of curvature of charged particles within the magnetic field. This can be used to determine the momentum of the particles. A more detailed description of the drift chambers can be found in Ref. [33].

2.3.4 Time-of-flight System

The time-of-flight (TOF) system is made up of scintillator paddles that form a shell around the drift chambers. Produced particles interact with the scintillators creating photons which are collected by photomultiplier tubes. The TOF system is used to gather information about the timing and energy of the particles produced by the reaction. A more detailed description of the TOF system can be found in Ref. [34].

2.3.5 Electromagnetic calorimeters

The electromagnetic calorimeters (EC) reside outside the TOF system and are used to detect neutral particles. The EC is a series of scintillators and lead sheets placed upon photomultiplier tubes. Neutral particles interact with a sheet of lead producing radiation which is amplified by a sheet of scintillator material. This process is repeated over numerous layers of lead and scintillators until the emitted photons reach the photomultiplier tubes which can convert them into a current.A more detailed description of the electromagnetic calorimeter can be found in Ref [35].

3 Data Analysis

The following chapter describes the data analysis carried out. This analysis built upon a previous analysis carried out on the Σ hyperon [36].

3.1 Overview

The overall aim of this analysis was to extract the beam spin asymmetry Σ for the product particles in the reaction of interest. Before Σ can be extracted, unwanted events must first be removed from the g13b data. This was done by using a series of cuts, each of which are described in the following sections. After applying the cuts Σ can be extracted using a maximum likelihood method. Once a technique of extracting Σ was established, Σ was studied in more detail by identifying kinematic regions where the results can be more specific.

3.2 Particle identification

The first cut applied was the particle identification cut. Particle identification was done by comparing the β value (particle velocity divided by the speed of light) of each track. The β value is equivalent to momentum divided by energy and can be measured in two different ways (shown in Eq. 1 and Eq. 2); one method used the information collected by the drift chamber and the other used the TOF system.

$$\beta_{DC} = \frac{p}{\sqrt{p^2 + (m^i_{PDG}c^2)^2}} \tag{1}$$

Eq. 1 shows how β_{DC} was calculated using drift chamber measurements, where m^i_{PDG} is the PDG mass (the drift chamber calculations are done under the assumption of either a K^+ or π^-) for each nominated candidate (K^+ or π^-). These measurements used the momentum of the tracks. In contrast, Eq. 2 shows how distance and time were used for the β_{TOF} calculation.

$$\beta_{TOF} = \frac{d_{TOF}}{(t_{TOF} - t_{start})c} \tag{2}$$

The difference between both independent calculations is simply given by $\Delta\beta = \beta_{DC} - \beta_{TOF}$. This allowed the testing of the earlier assumption of m^i_{PDG}, since the correct events lie around $\Delta\beta = 0$. This can be seen in Fig. 11 which shows $\Delta\beta$ as a function of momentum before any cuts have been applied to it. Fig. 11 shows the $\Delta\beta$ momentum dependence for events which have a single positive and negative track. Since the events of interest only have a single K^+ and a single π^-,

the positive tracks are assigned the nominal mass of K^+ and similarly the negative tracks are assigned the nominal mass of π^-.

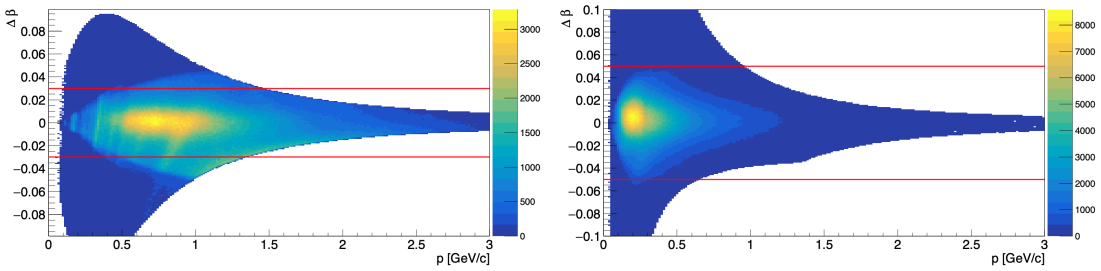

Figure 11: Example of $\Delta\beta$ momentum dependence for the positive, assumed to be a K^+ track (left) and the negative, assumed to be a π^- track (right). The red lines indicate cuts yet to be applied. The shapes seen on the plots (for example the shoulder just below p=1.5 GeV on the right panel) are produced by cuts previously applied to the data during skimming. During skimming, wide $\Delta\beta$ cuts were applied onto the data set to reduce file size.

The pattern of the left panel of Fig. 11 indicated that a large number of out-of-time π^+ particles are being wrongly identified as kaons. Cuts applied to the $\Delta\beta$ distributions reduce these misidentifications. Further cuts, as described in Sec. 3.3 and 3.5, also contributed towards the reduction of this issue.

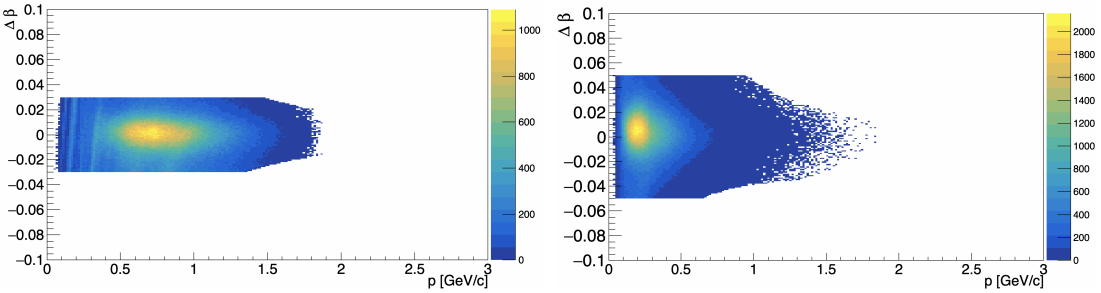

Figure 12: Example of $\Delta\beta$ momentum dependence for the positive, assumed to be K^+ track (left) and the negative, assumed to be π^- track (right), after applying a cut on $\Delta\beta$.

3.3 Photon selection

The photon selection cut identifies the photon that initiated the reaction. This is done by comparing the timing information gathered by the tagger (t_γ) with that of the CLAS detector (t_{track}). Tagger information ascertains the time at which the photon is absorbed, whereas CLAS determines the time at which the reaction begins. For the same photon, the difference between the two should be 0.

$$\Delta t = t_{track} - t\gamma \tag{3}$$

Multiple electrons are detected in coincidence with the event being detected in CLAS. Fig 13 shows the distribution of coincidence times of K^+ and π^- events (left and right respectively) with the event detected by the tagger. The events of interest lie around $\Delta t = 0$ therefore a cut described as $|\Delta t_{K^+/\pi^-}| < 1$ is placed on the coincidence time of both the K^+ and π^- events.

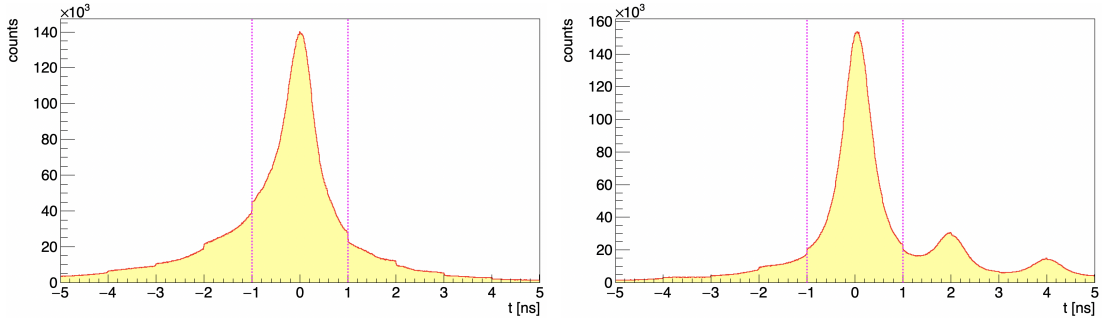

Figure 13: Distributions of the coincidence times of the photon detected in the tagger and K^+/π^- events (left/right respectively) detected in CLAS. All other reaction reconstruction cuts (described in the following sections) have been applied and the photon selection cut is shown by the dashed lines.

3.4 Photon polarisation

As discussed in Sec. 2.2.1, the experimental procedure during the g13b run period involved using linearly polarised photons. Photons with energies close to the coherent edge have smaller systematic uncertainties with respect to the degree of polarisation. To remove larger uncertainties, a cut was applied on the photon energies regarding the coherent edge. E_γ was required to be within 200 MeV of the coherent edge (Coh Edge - 200 MeV < E_γ < Coh Edge). Further to this, the degree of polarisation was also taken into account. As mentioned in Sec. 2.2.1, the degree of polarisation as a function of photon energy was summarised in lookup tables. This information was incorporated into the analysis. A cut was also set on the photon polarisation, only allowing events with $P_\gamma > 0.5$, since these events also have smaller associated uncertainties.

3.5 Particle misidentification

As shown in Fig. 11 a portion of out-of-time π^+ particles were misidentified as kaons. Even after the cuts described in Sec. 3.2 and 3.3, these misidentifications could still be found. The remaining misidentified events were mostly removed by applying a simple cut on the missing mass of the $\gamma n \to \pi^+\pi^- X$ reaction. For misidentified events, the missing mass would correspond to a nucleon

mass. The missing mass of $\gamma n \to \pi^+\pi^- X$ could be plotted against the missing mass of the reaction of interest $\gamma n \to K^+\pi^- X$. For the reaction of interest, the correct events would have a missing mass consistent with that of a nucleon.

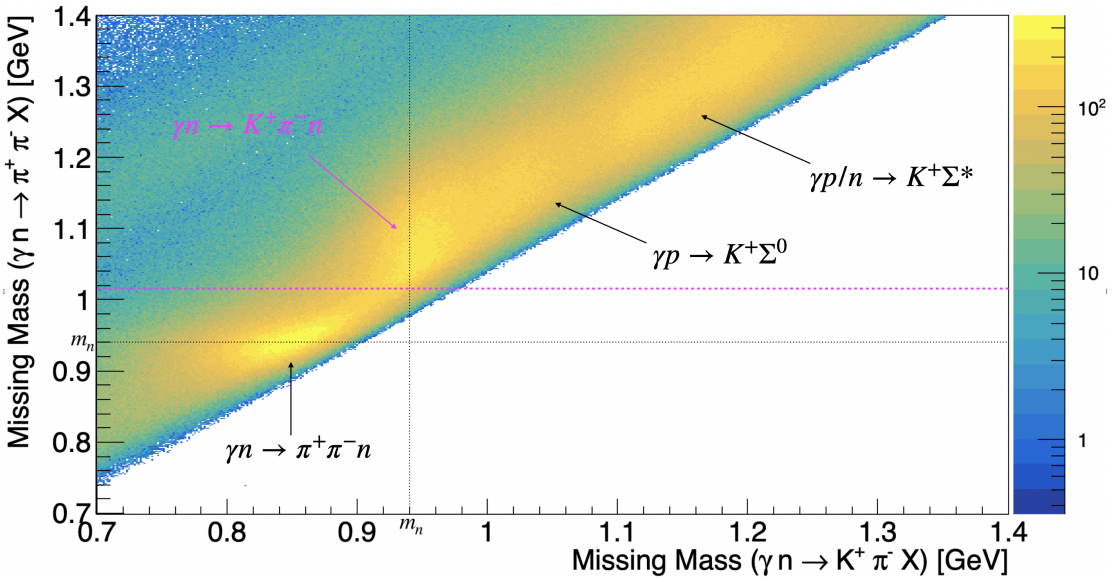

Figure 14: Missing mass of $\gamma n \to \pi^+\pi^- X$ as a function of the missing mass of $\gamma n \to K^+\pi^- X$. The horizontal line indicates the position of the cut applied to remove the misidentified pion events.

The events of interest have MM($\gamma n \to K^+\pi^- X$) around 0.94 GeV/c^2. The misidentified pion events lie further down the 2D plot, at MM($\gamma n \to K^+\pi^- X$) around 0.85 GeV/c^2. The pink horizontal line shown on Fig. 14 represents a cut that can be applied to the missing mass of $\gamma n \to \pi^+\pi^- X$. This cut removes any data with MM($\gamma n \to \pi^+\pi^- X$) < 1.015 GeV/$c^2$.

The cut described in this section was tight to ensure that contributions from misidentified pions were minimised. The effect that the location of the cut has on the final determination of the polarisation observable is further explored in Sec. 4.

3.6 Reaction reconstruction

The cuts previously described have ensured that positive tracks equate to K^+ particles and negative to π^- particles. A 2D elliptical cut can be applied to remove background contributions. Before the cut can be applied, the events of interest must be identified. This was done by examining the missing mass of $\gamma n \to K^+\pi^- X$ and the invariant mass of Σ^-. Fig. 15 is a 2D plot showing the distribution of both of these values. For events of interest, MM($\gamma n \to K^+ X$) should correspond to the mass of the spectator proton (0.938 GeV) and IM(Σ^-) should lay around 1.197 GeV.

The two-dimensional elliptical cut is described by Eq. 4:

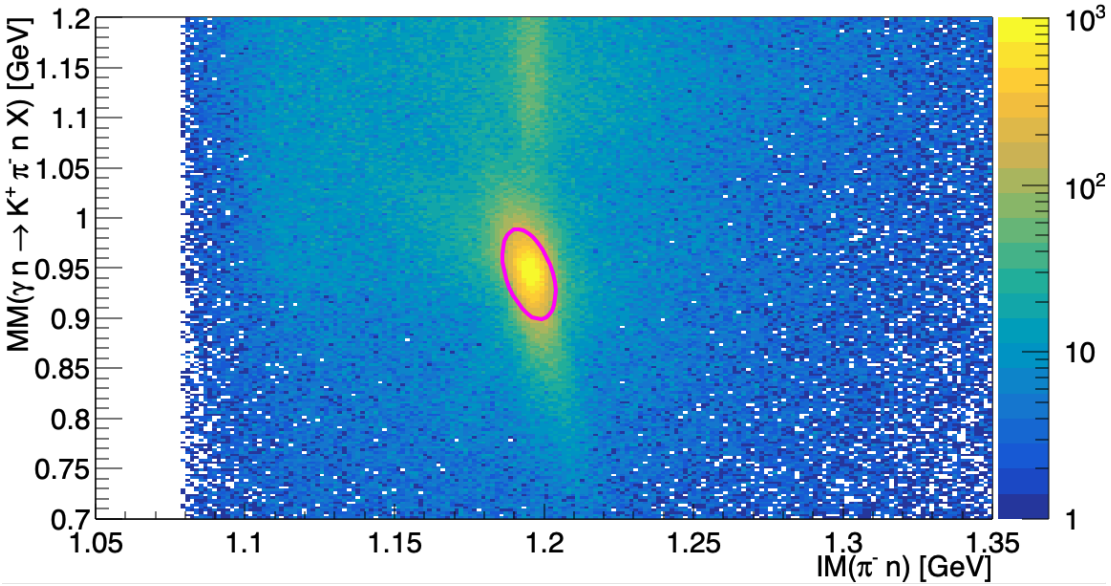

Figure 15: Missing mass of $\gamma n \rightarrow K^+\pi^- nX$ vs invariant mass of Σ^-. The 2D elliptical cut is represented by the pink ellipse.

$$\frac{[x'Cos(\alpha) - y'Sin(\alpha)]^2}{R_a^2} + \frac{[x'Sin(\alpha) + y'Cos(\alpha)]^2}{R_b^2} < 1 \tag{4}$$

where $\alpha = 45°$, $R_a = 0.008$, $R_b = 0.045$, $x' = x - 1.195$ and $y' = y - 0.944$ were used to remove background contributions, from other reactions such as $\gamma p \rightarrow K^+\Lambda$ and $\gamma p \rightarrow K^+\Sigma^0$ *.

The effects of the background cut can be seen in Fig. 16, where the blue lines indicate the respective distributions before the elliptical cut and the red lines indicate after the cut has been applied. In both plots, the majority of the background signal was removed while still keeping the majority of the correct data points. Fig. 16 improves confidence in the elliptical cut, however, the size of the ellipse is explored in more detail in Sec. 4.6.

*These other reactions can be seen in Fig. 15 as areas outside of the events of interest with high statistics. Ref. [36] explores the background contributions in more detail.

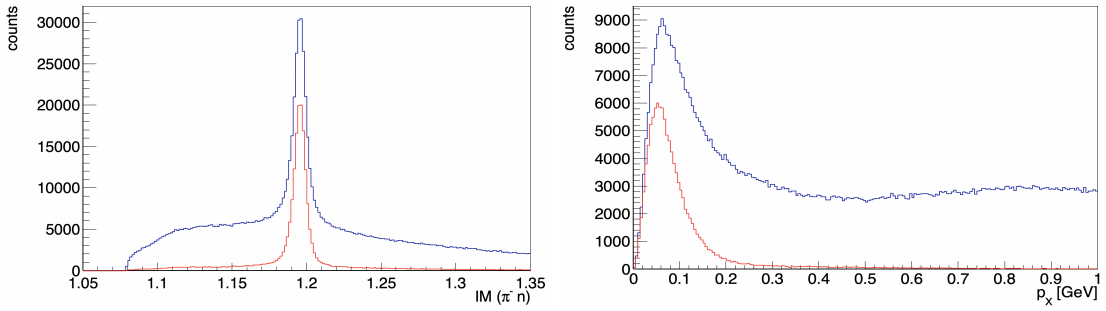

Figure 16: The invariant mass of Σ^- (left) and the missing momentum of the spectator proton (right). The blue lines show the plots before the elliptical cut was applied and the red lines show after the cut has been applied.

3.7 Beam spin asymmetry Σ

The beam spin asymmetry, represented by Σ (not to be confused with the Σ^- particle), is a polarisation observable acquired from the differential cross-section equation for the photoproduction of mesons from an unpolarised target with a polarised photon beam:

$$\frac{d\sigma}{d\Omega} = \left(\frac{d\sigma}{d\Omega}\right)_0 [1 - P_{lin}\Sigma\cos(2\phi)] \tag{5}$$

where Ω is the solid angle and P_{lin} is the transverse polarisation of the beam at an angle ϕ to the reaction plane (seen in Fig. 17).

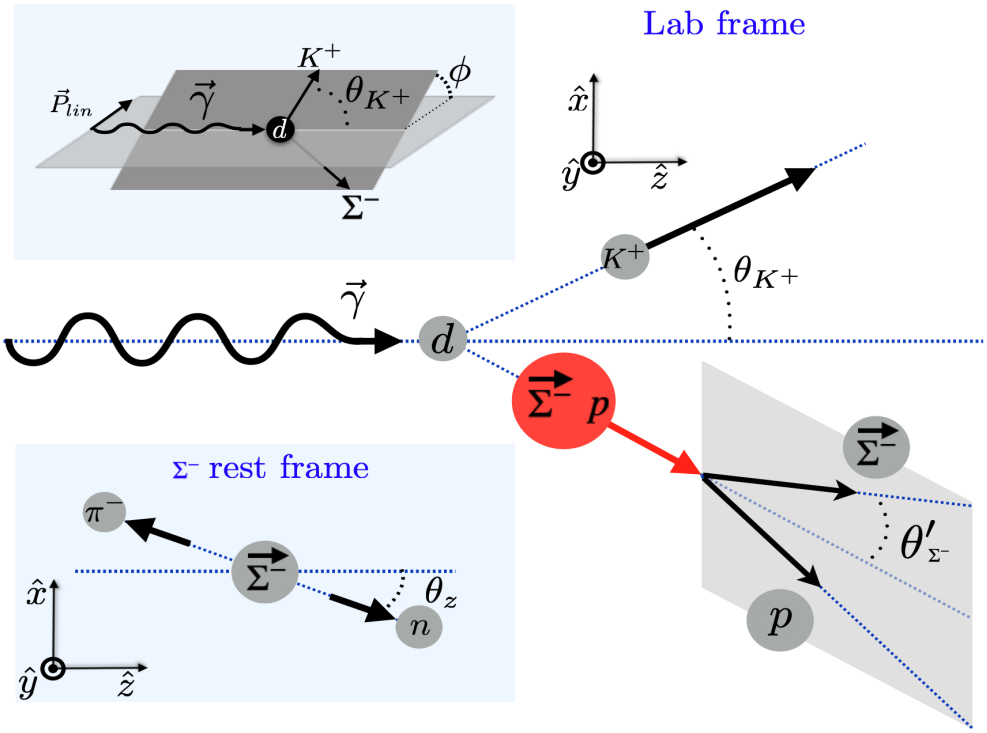

Figure 17: A diagram depicting the reaction of interest in the lab frame. The diagram also shows how the angles ϕ and θ relate to the reaction plane [37].

Σ provides information about the preferential direction of an interaction. A large value in Σ indicates that the associated particle has a strong preference in its direction of scatter (provided the particle was produced by a polarised photon beam). Any further interaction undergone by the particle changes the direction of travel, thereby diluting the magnitude of Σ. In this analysis, Σ was extracted for the K^+ and Σ^- particles as well as for the spectator proton. Σ was extracted independently for each particle, allowing the comparison between particles.

The Σ corresponding to the spectator proton was extracted with the aim of isolating events where the spectator interacts. As well as this, the dynamics of this reaction should lead to the spectator proton having an associated Σ equal to 0. Results consistent with this expectation further increase confidence in the quality of the analysis.

3.7.1 Determination of Σ

The extraction of the polarisation observable Σ was undertaken using two independent techniques, both based on a maximum likelihood method previously developed and proven to produce

reliable results by other previous analyses [38][39][40][36]. The maximum likelihood estimation is a well-established statistical technique that determines a value by maximising the likelihood of a statistical model being correct. Both a binned maximum likelihood and unbinned maximum likelihood technique were used for this analysis. Using both techniques allows a comparison between the two, since individual results can be visually inspected. It also increases confidence in the final results if both separate techniques output the same results.

The maximum likelihood method requires the use of a log-likelihood function, which varies slightly for the binned and unbinned methods. Both log-likelihood functions were derived from the differential cross-section equation (Eq. 5).

3.7.2 Binned maximum likelihood technique

$$\log L_b(E_\gamma, \cos\theta_{K^+}, p_x) = \sum_i \log\left(1 - P^i_{lin}\Sigma\cos(2\phi_i)\right) \tag{6}$$

The log-likelihood equation for the binned technique is a function of photon energy, the K^+ scattering angle and the momentum of the spectator proton. This technique required the data to be binned in the missing momentum of the spectator proton.

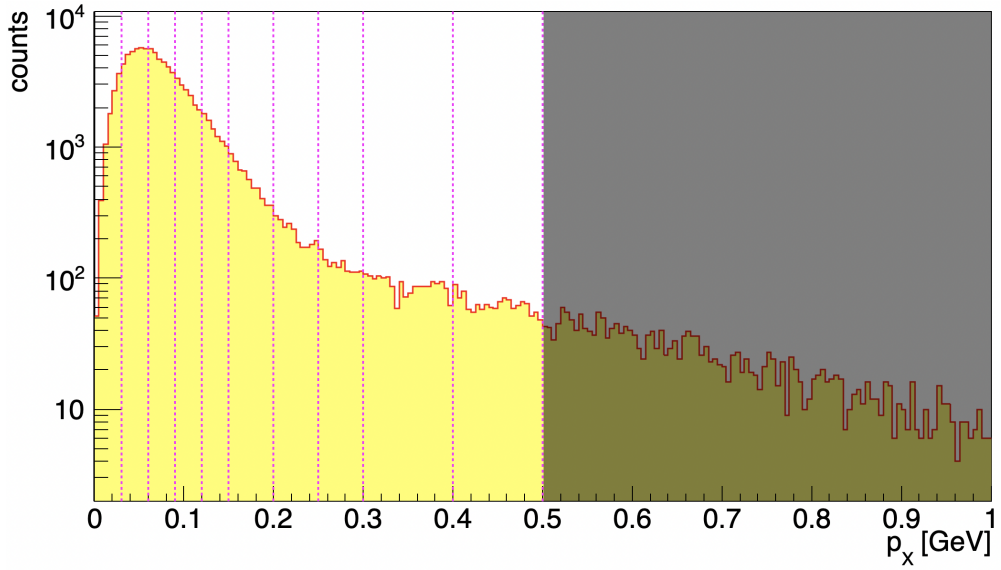

Figure 18: The distribution of the missing momentum of the spectator proton after all the cuts were applied.

Fig. 18 shows the distribution of the missing momentum after all cuts were applied, which peaks below 0.1 GeV. Hardly any data is seen above 0.5 GeV. For this reason, ten data bins were used,

with a finer binning at lower missing momentum and wider bins up to a highest missing momentum up to 0.5 GeV. Using the binned log-likelihood function (Eq. 6), the beam spin asymmetry Σ could be extracted with an associated uncertainty for each missing momentum bin.

The beam spin asymmetry was then plotted as a function of the missing momentum, and a fit applied to the ten points (corresponding to each bin). An example plot can be seen in Fig. 19.

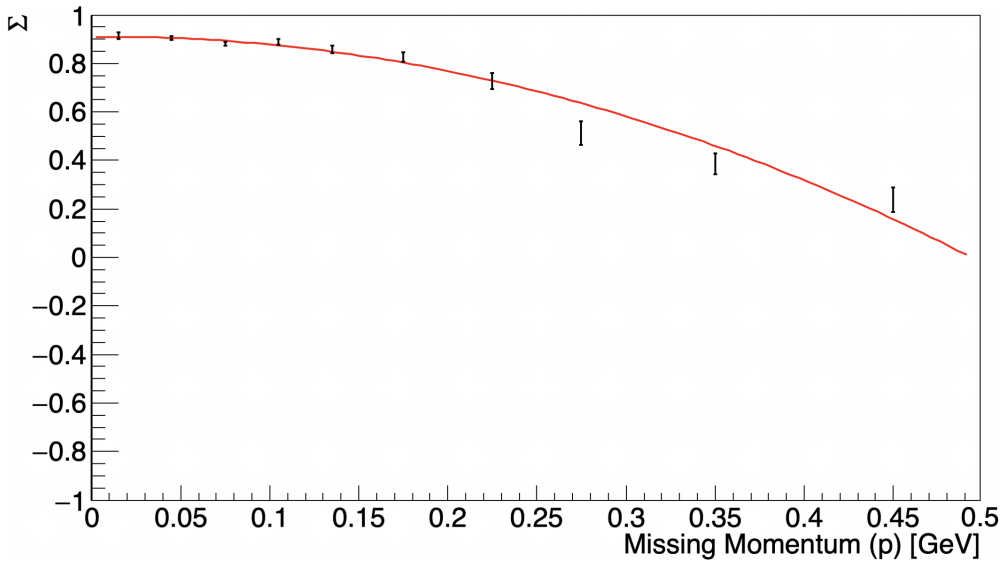

Figure 19: An example plot of Σ vs missing momentum of the spectator proton extracted using the binned technique. The black bars represent each missing momentum bin and the associated error bars. The red line is a fitting placed on the black bars.

3.7.3 Unbinned maximum likelihood technique

$$\log L_u(E_\gamma, \cos\theta_{K^+}) = \sum \log\left(1 - P_{lin}^i f(x)\cos(2\phi_i)\right) \tag{7}$$

$$\text{where } f(x) = a + bx^2 + cx^{3\dagger}$$

The log-likelihood equation for the unbinned technique is a function of photon energy and the K^+ scattering angle. The unbinned maximum likelihood technique, as suggested by its name, required no binning of the data. The unbinned maximum likelihood equation replaces Σ from

†The linear term was not included in order to ensure a maximum at zero missing momentum. After taking the differential $\frac{df(x)}{dx} = 2bx + 3cx^2$ it can be seen how the gradient of the function is equal to zero when the missing momentum of the spectator, x = 0
and x = missing momentum of the spectator proton

the binned likelihood equation with a predetermined function, which is dependant on the missing momentum of the spectator proton. While the form of the function is already set, the parameters of the function were extracted by the analysis. The completed function is equivalent to Σ and was plotted as such.

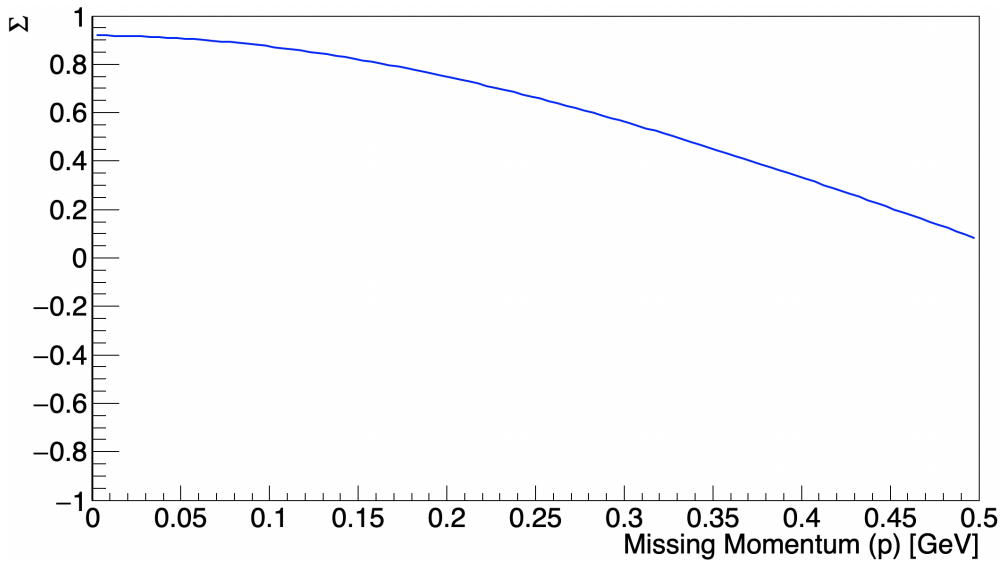

Figure 20: An example plot of Σ vs missing momentum of the spectator proton extracted using the unbinned technique. The red line is the completed function $f(x)$ shown in Eq. 7.

3.8 Bootstrapping

The nature of the binned technique meant the uncertainties associated with the determination of Σ were incorporated within the results. The unbinned technique required an extra step to assess the uncertainties. The bootstrapping technique allowed for the computation of the uncertainties for the unbinned technique. Bootstrapping is an established statistical technique [41] that allows a single data set to be remade into many simulated data sets. By resampling but allowing for repetition, many new samples can be created from one original sample, which in turn allows for a distribution of statistics.

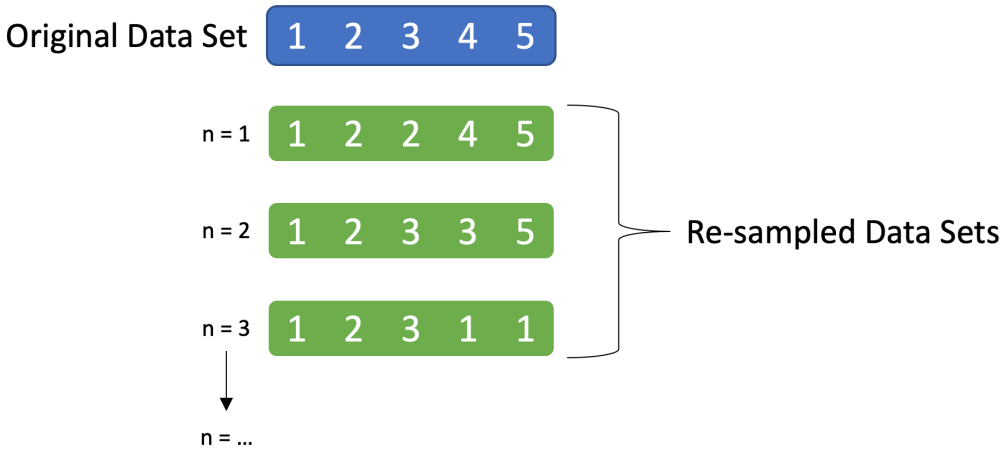

Figure 21: A generic diagram showing how the bootstrapping method could re-sample a very simple data set.

For this analysis, the data was resampled 200 times and Σ was recalculated using the unbinned technique for each iteration. All 200 iterations of Σ were then compiled into one histogram. The bootstrapping method allows a visualisation of the uncertainties in Σ while using the unbinned technique.

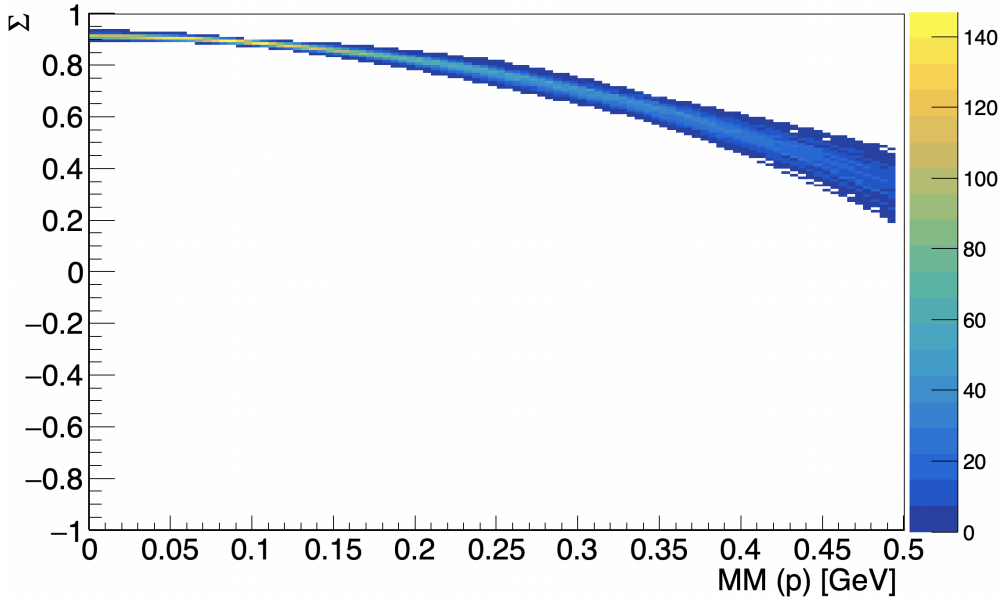

Figure 22: An example of a plot produced by the bootstrapping method. A wider section of the plotted function corresponds to a larger associated uncertainty in Σ. This technique produced a visual representation of the uncertainties associated with the unbinned technique.

3.9 Two-fold binning

The g13b data can be binned in both photon beam energy (E_{gamma}) and the scattering angle of the K^+ in the centre of mass frame ($\cos\theta^{c.m.}_{K^+}$) (shown in Fig. 17). A visual representation of the spread of data and the binning applied is shown in Fig. 23.

Binning in both E_γ and $\cos\theta^{c.m.}_{K^+}$ allowed the identification of specific kinematic regions where Σ^- interactions dominate. This could be seen in areas where the beam spin asymmetry had an increased dilution for the Σ^- particle. Additionally, the two-fold binning approach gave access to specific bins within which the number of events were higher. A bin with a higher number of events corresponds to lower associated uncertainty in Σ. The full results obtained from the two-fold binning can be found in Sec. 5.0.2.

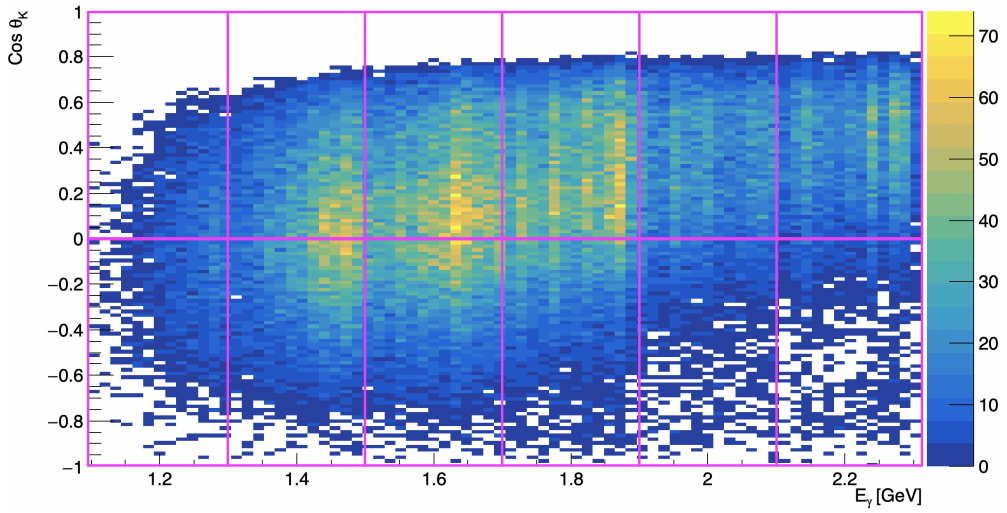

Figure 23: A plot showing all the available data after all cuts were applied. The pink grid represents the binning applied on both E_γ and $\cos\theta^{c.m.}_{K^+}$.

4 Systematic Studies

Systematic uncertainties may arise from the positioning of the cuts applied during the particle identification and reaction reconstruction sections of the analysis. They also arise from the degree of photon polarisation. This chapter details the investigations into the systematic effects of each of the cuts applied.

The systematic uncertainties were studied by examining the differences of the extracted polarisation observables from the nominal cuts used during the analysis, Σ_{nom}, and either a tighter or looser cut, $\Sigma_{t/l}$. The uncertainties of observables from the nominal and tighter/looser cuts are heavily correlated since both sets are determined from the same data set, hence the difference $\Delta\Sigma = \Sigma_{nom} - \Sigma_{t/l}$ reflects the systematic effects. The difference $\Delta\Sigma$ was studied as a function of E_γ and was found for all $\cos\theta^{c.m.}_{K^+}$.

Each of the following studies have 2 sets of plots, one set for the binned technique and another for the unbinned. The calculation of systematic effects for the binned and unbinned techniques utilised slightly different methods.

4.0.1 Systematic effects when using the binned maximum likelihood technique

For the binned technique, the difference $\Delta\Sigma$ between the nominal cut and either a tighter or looser cut for each missing momentum bin was calculated. These differences are then plotted as a function of photon energy. The various coloured points on the binned plots correspond to the different missing momentum bins. An upper estimate is provided on each of the systematic plots. Since the determined observables ($\Sigma_{t/l}$ and Σ_{nom}) are heavily correlated to one another, systematic effects and statistical fluctuations are difficult to distinguish. The upper estimate for each systematic study encompasses both systematic errors and statistical fluctuations. The upper estimate for each systematic study is equal to the average value added to the RMS value of $\Delta\Sigma$: $|\bar{\Delta\Sigma}| + RMS_{\Delta\Sigma}$.

4.0.2 Systematic effects when using the unbinned maximum likelihood technique

The systematic effects are processed in a different manner for the unbinned technique. The difference ($\Delta p_{a/b/c}$) between the nominal cut and either a tighter or looser cut for each returned parameter of the unbinned function (Eq. 7) was calculated.

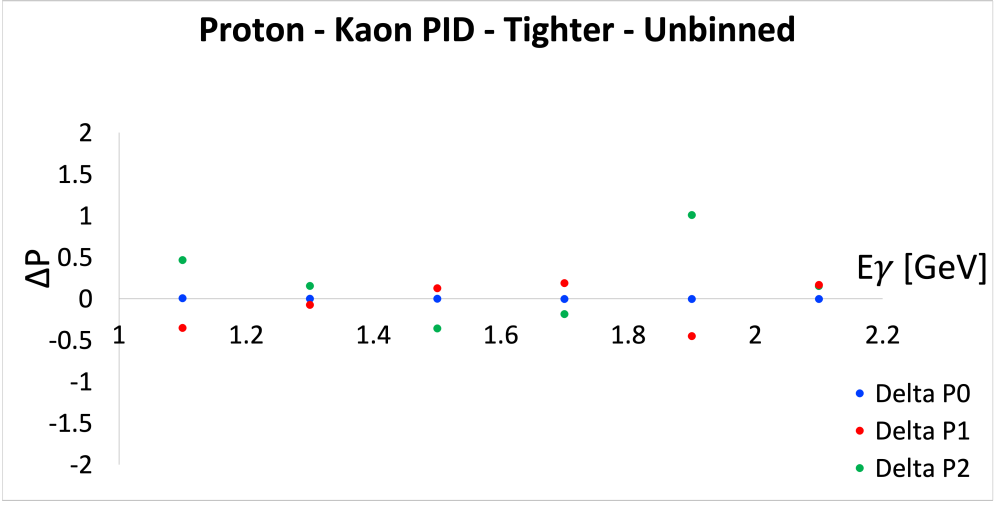

Figure 24: An example of $\Delta p_{0/1/2}$ as a function of E_γ for the Σ^- particle in the kaon particle identification systematic study. $\Delta p_{0/1/2}$ can be re-inserted into the pre-determined unbinned function in order to output the final results of the unbinned technique systematics.

An example of $\Delta p_{0/1/2}$ as a function of E_γ can be seen in Fig. 24. For each photon energy bin, $\Delta p_{0/1/2}$ can then be reinserted into Eq. 7 and plotted as a function of the missing momentum to give a better visual representation of the associated systematic uncertainties.

4.1 Systematic effects of particle identification

4.1.1 Kaon PID

The cut for the kaon particle identification cut was varied from a nominal cut of $|\Delta\beta| < 0.03$ was compared to a tighter cut of $|\Delta\beta| < 0.025$ and a looser cut of $|\Delta\beta| < 0.035$. The larger uncertainties were seen with the tighter cut.

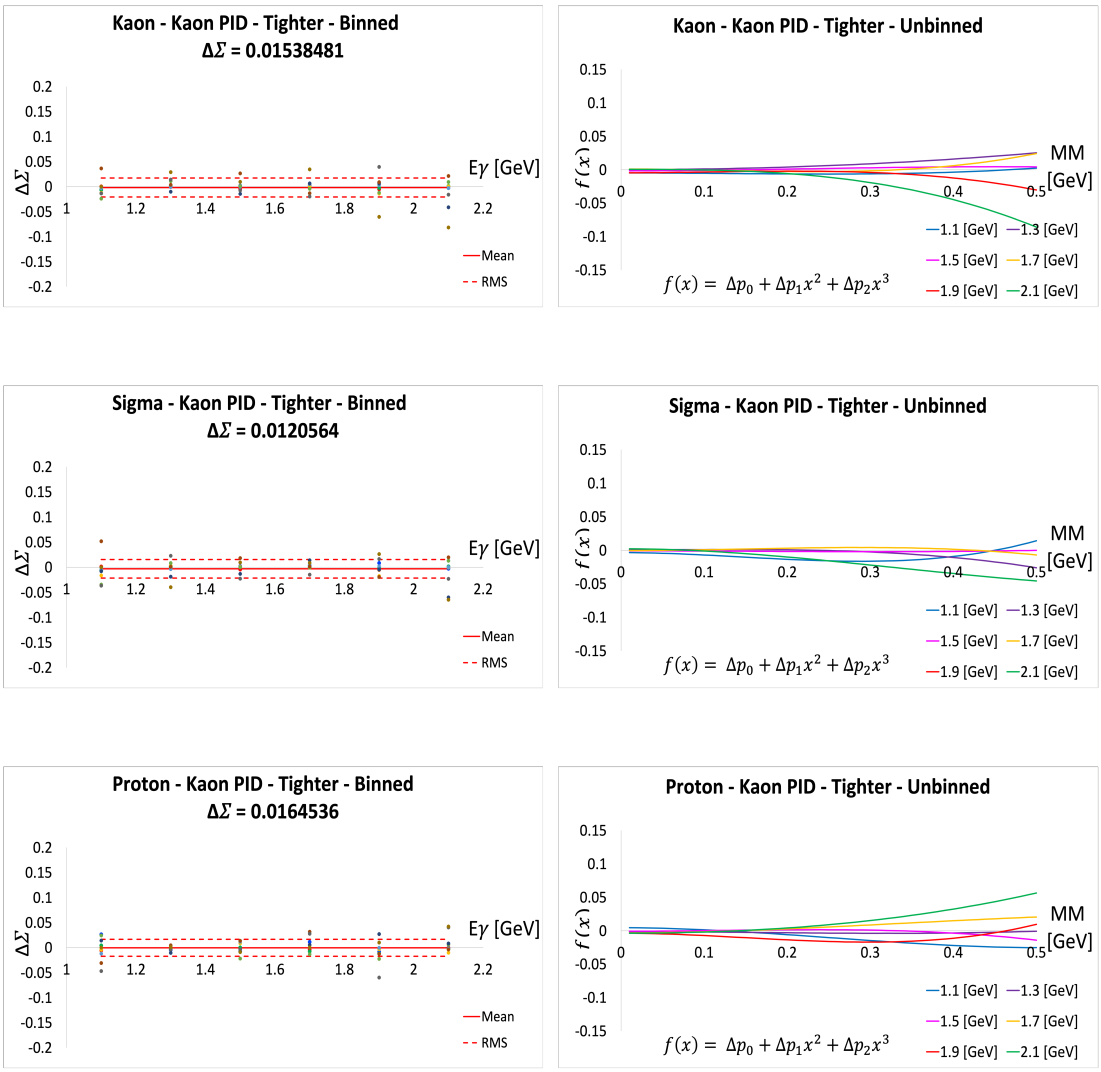

Figure 25: Systematic uncertainties associated with the kaon particle identification cut.

4.1.2 Pion PID

The cut for the pion particle identification cut was varied from a nominal cut of $|\Delta\beta| < 0.05$ was compared to a tighter cut of $|\Delta\beta| < 0.041$ and a looser cut of $|\Delta\beta| < 0.059$. The larger uncertainties were seen with the tighter cut.

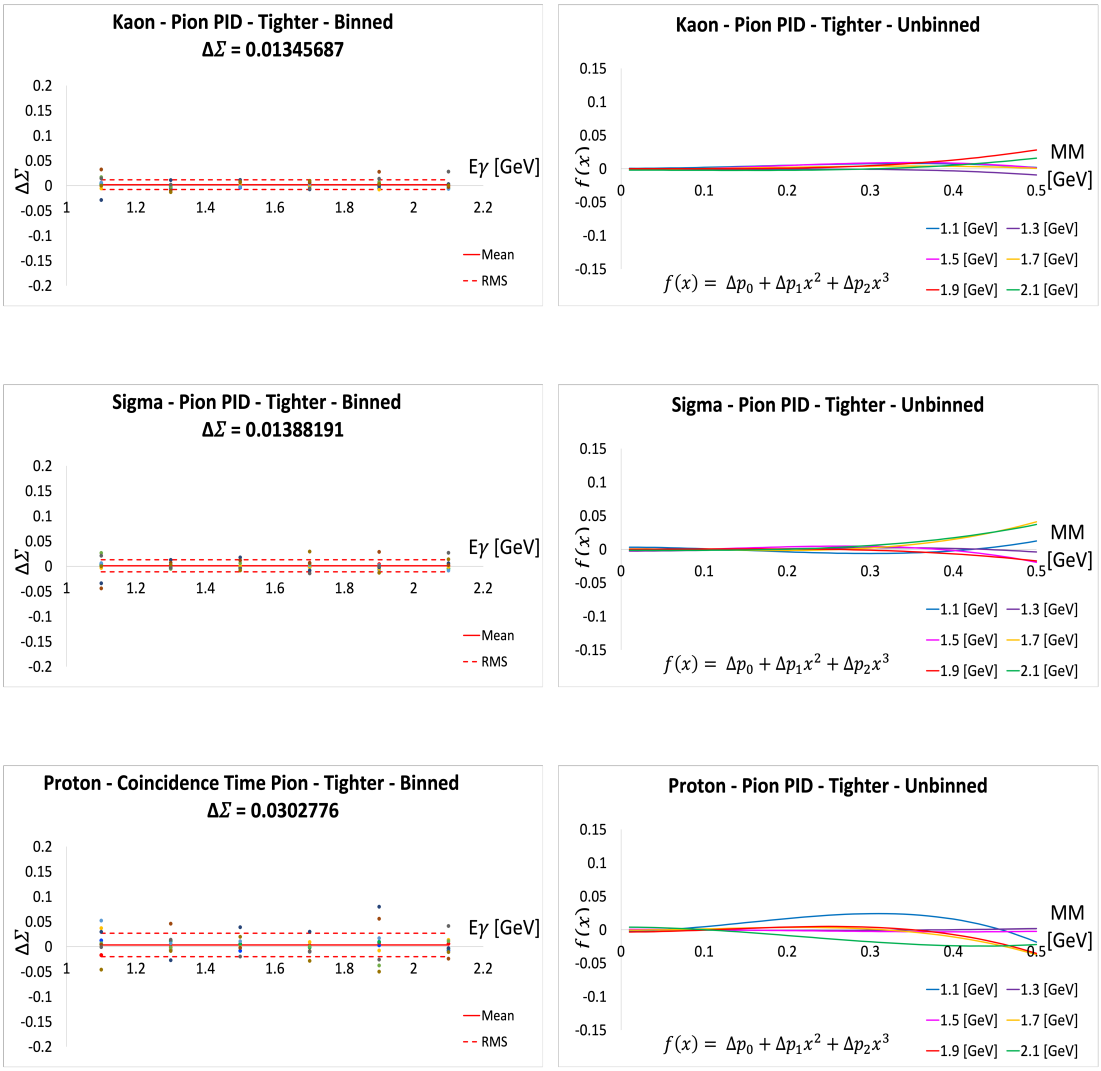

Figure 26: Systematic uncertainties associated with the pion particle identification cut.

4.2 Systematic effects of photon selection

4.2.1 Kaon coincidence time

The cut for the the kaon coincidence time cut was varied from a nominal cut of $t = 1.0$ns was compared to a tighter cut of $t = 0.8$ns and a looser cut of $t = 1.2$ns. The larger uncertainties were seen with the tighter cut.

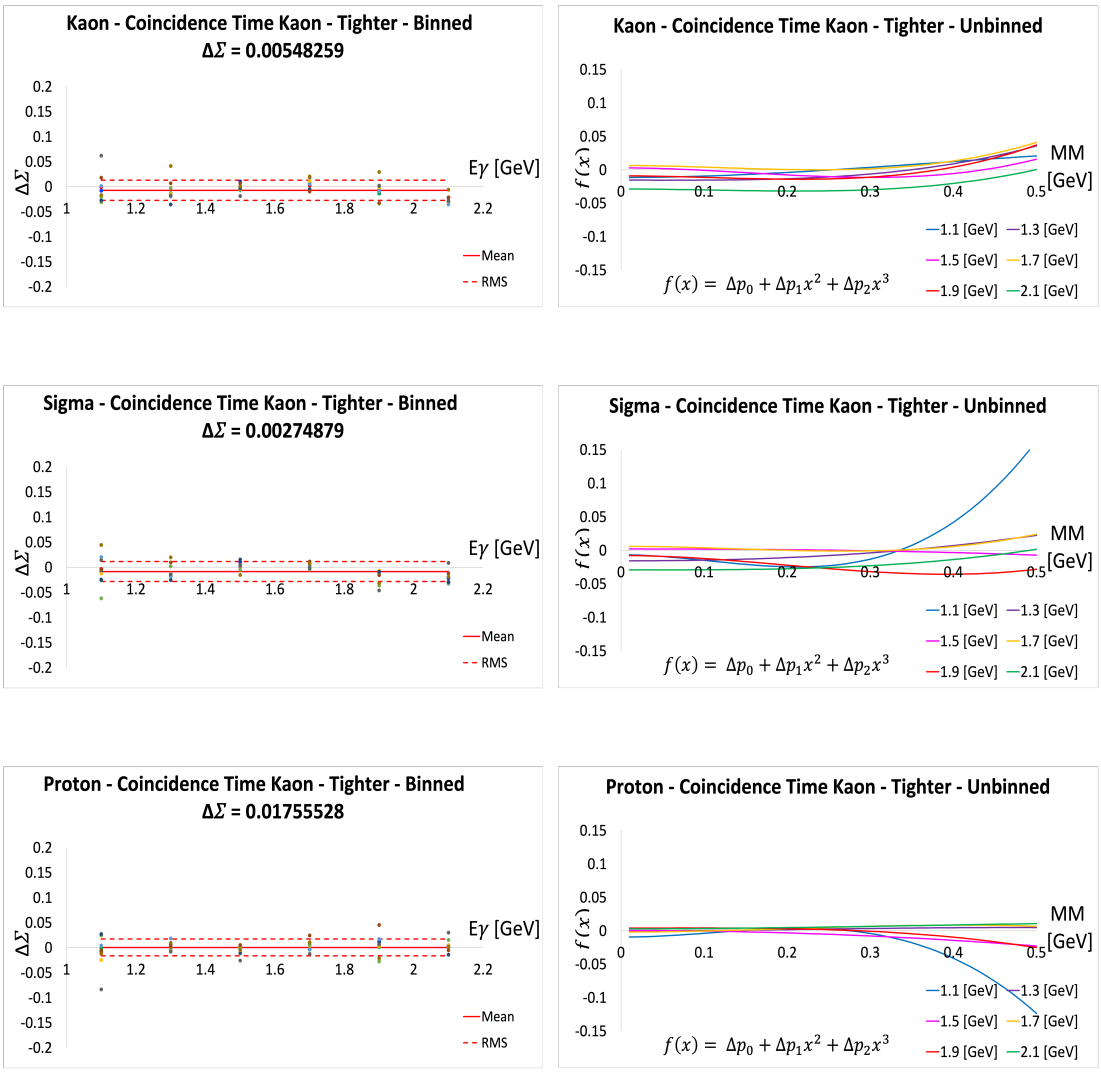

Figure 27: Systematic uncertainties associated with the kaon coincidence time cut.

4.2.2 Pion coincidence time

The cut for the the pion coincidence time cut was varied from a nominal cut of $t = 1.0$ns was compared to a tighter cut of $t = 0.8$ns and a looser cut of $t = 1.2$ns. The larger uncertainties were seen with the tighter cut.

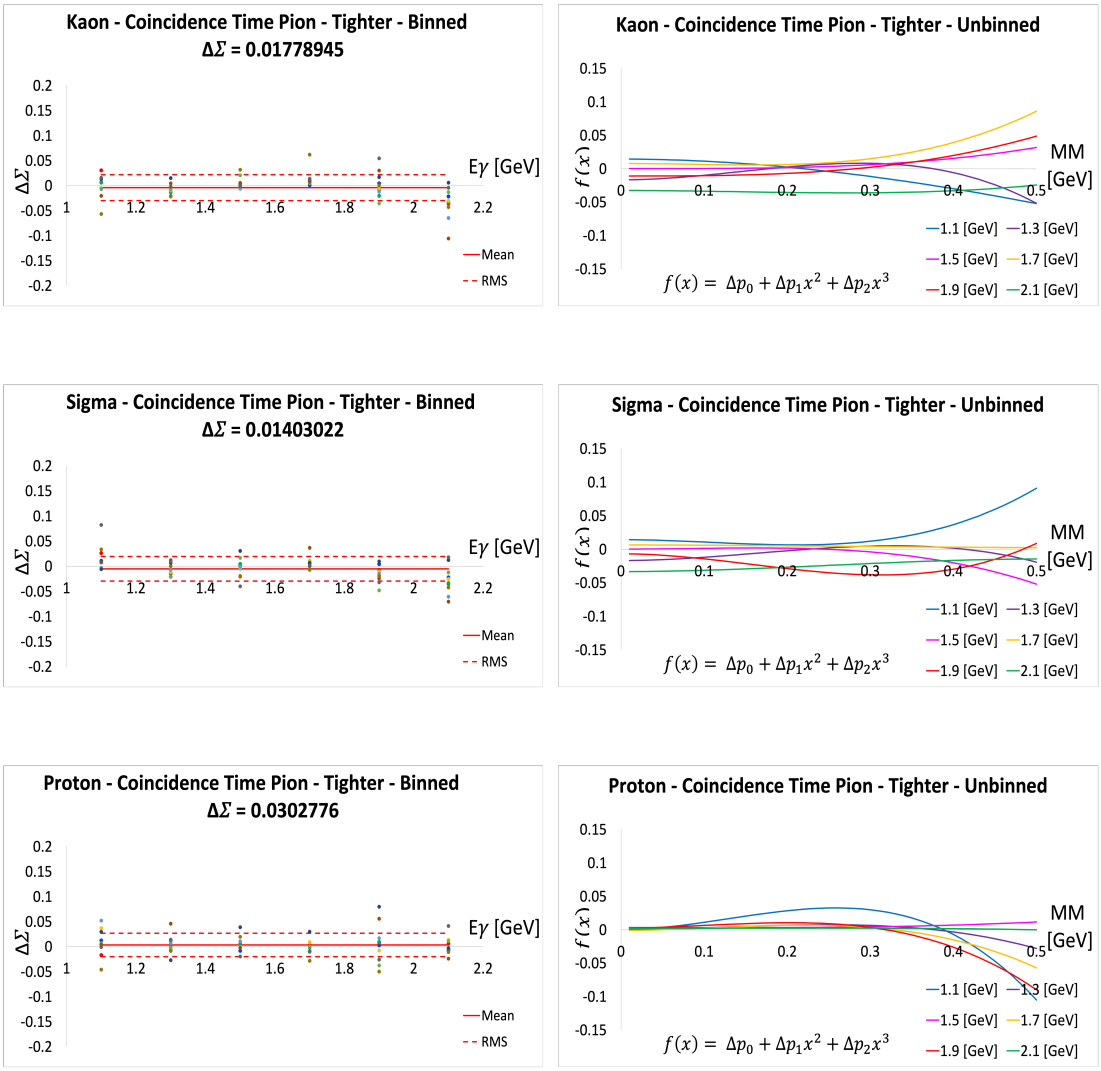

Figure 28: Systematic uncertainties associated with the pion coincidence time cut.

4.3 Systematic effects of photon polarisation

The cut on the coherent edge removed data outside of the nominal range Coh Edge - 200 MeV < E_γ < Coh Edge. This was compared to a tighter cut of Coh Edge - 195 MeV < E_γ < Coh Edge and a looser cut of Coh Edge - 205 MeV < E_γ < Coh Edge. The larger uncertainties were seen with the tighter cut.

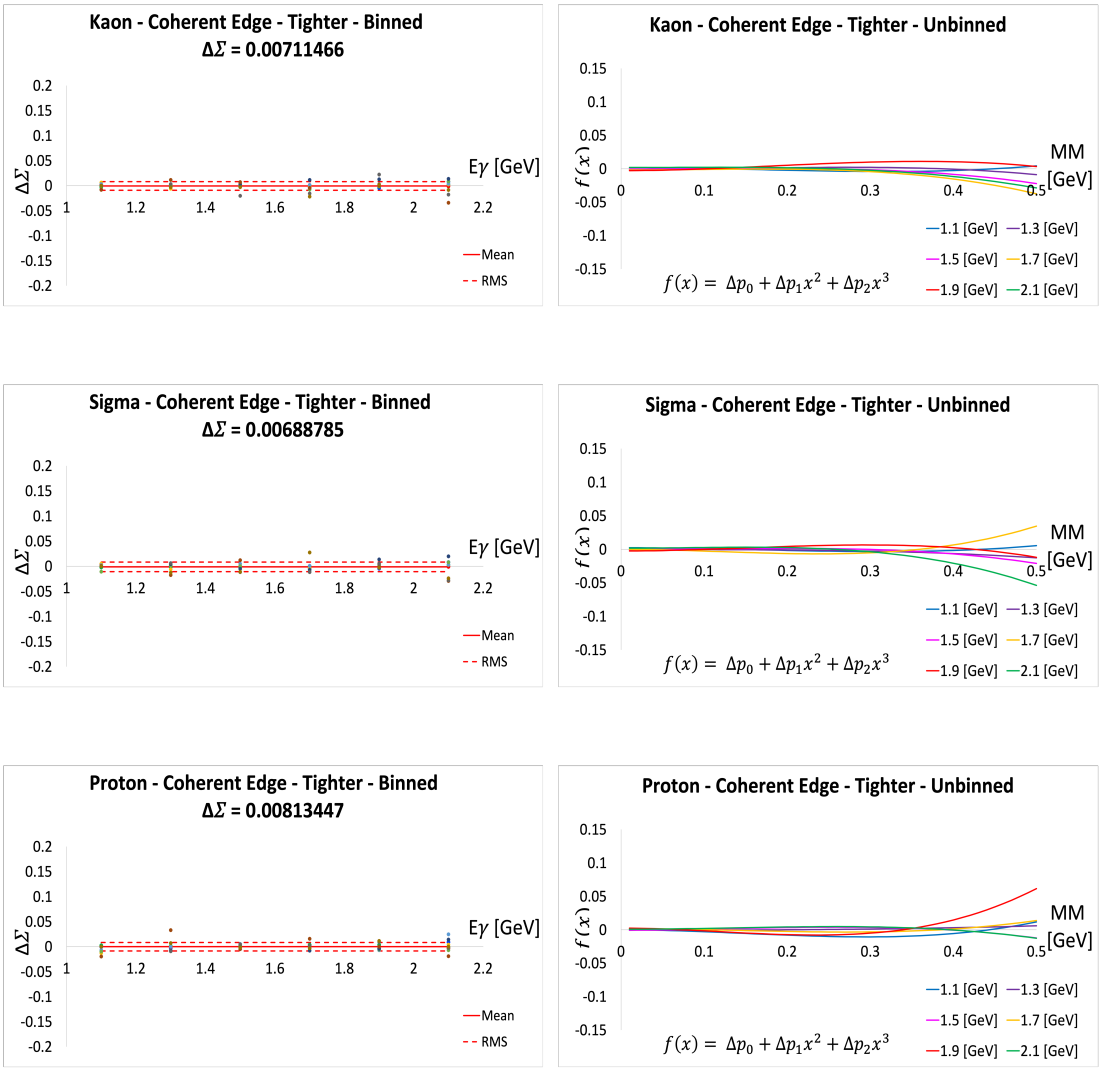

Figure 29: Systematic uncertainties associated with the coherent edge cut.

4.4 Systematic effects of particle misidentification

The particle misidentification cut removed data outside of the nominal range MM($\gamma n \rightarrow \pi^+\pi^- X$) < 1.015 GeV/$c^2$. This was compared to a tighter cut of MM($\gamma n \rightarrow \pi^+\pi^- X$) < 1.025 GeV/$c^2$ and a looser cut of MM($\gamma n \rightarrow \pi^+\pi^- X$) < 1.005 GeV/$c^2$. The larger uncertainties were seen with the tighter cut.

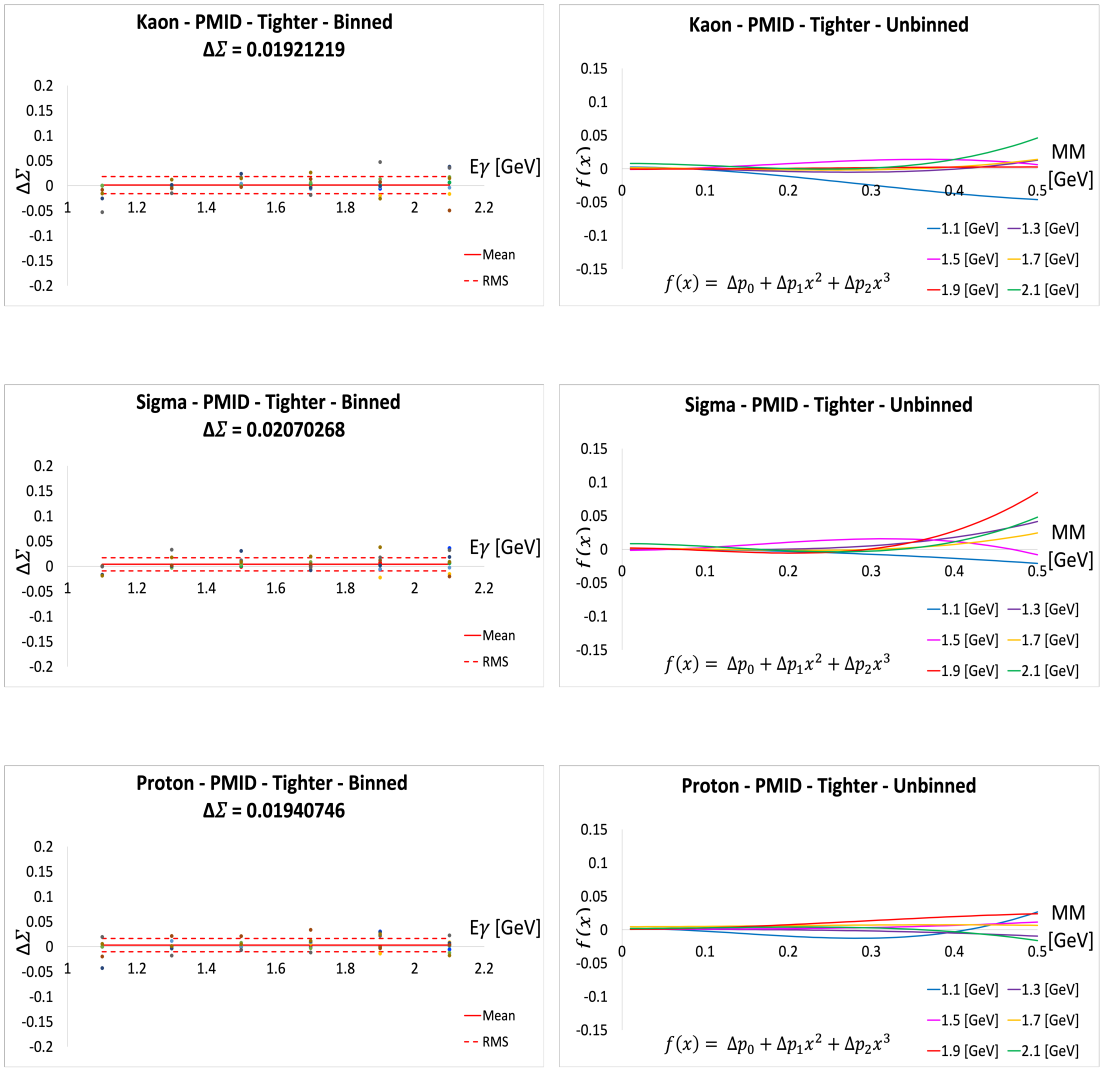

Figure 30: Systematic effects associated with the particle misidentification cut.

4.5 Systematic effects of the background removal cut

The elliptical background removal cut can be independently varied in both the x and y axes of the ellipse.

4.5.1 Ellipse x-axis

The cut for the the x-axis of the elliptical background removal cut was varied from a nominal cut of $R_x = 0.008$ was compared to a tighter cut of $R_x = 0.005$ and a looser cut of $R_x = 0.011$. The larger uncertainties were seen with the tighter cut.

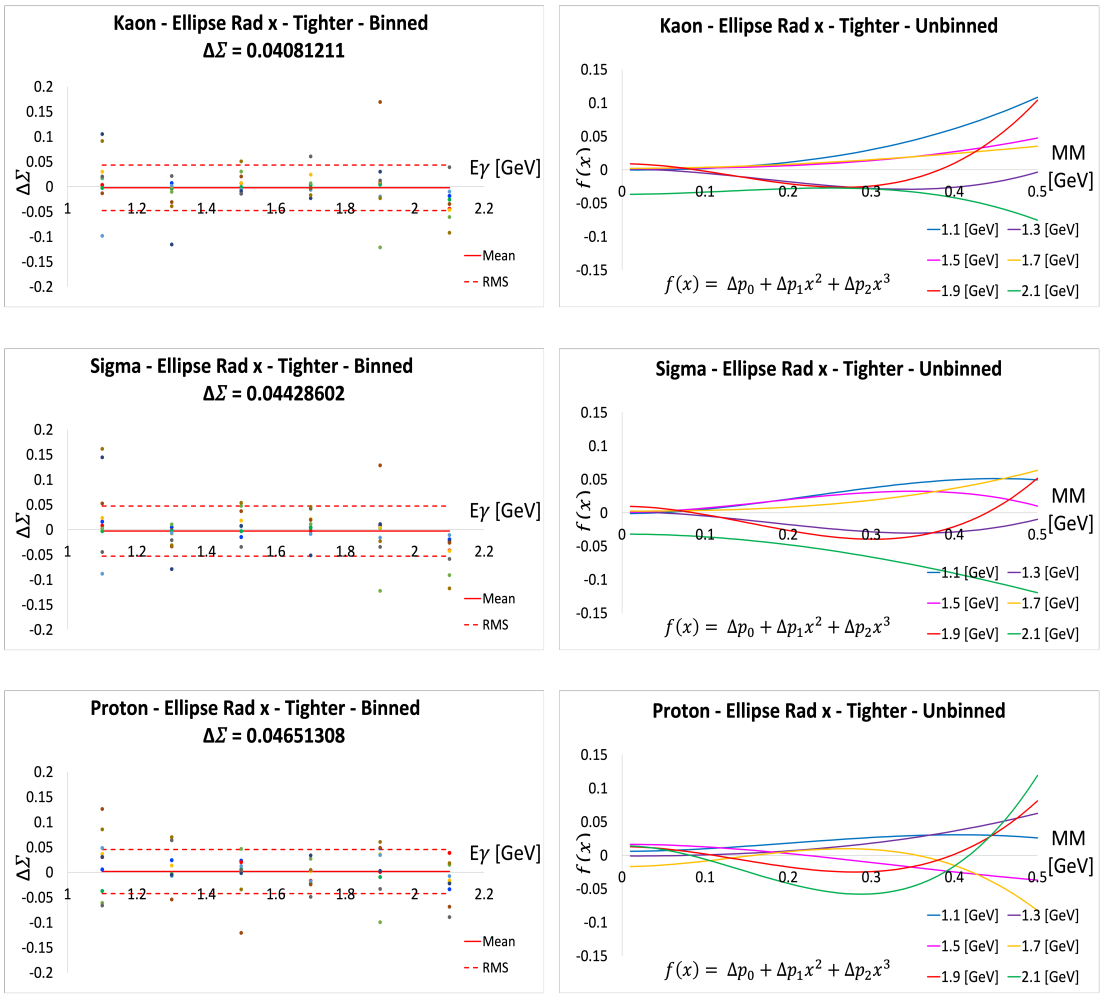

Figure 31: Systematic effects associated with the radius (in the x axis) of the elliptical cut.

4.5.2 Ellipse y-axis

The cut for the the y-axis of the elliptical background removal cut was varied from a nominal cut of $R_y = 0.045$ was compared to a tighter cut of $R_y = 0.0425$ and a looser cut of $R_y = 0.0475$. The larger uncertainties were seen with the tighter cut.

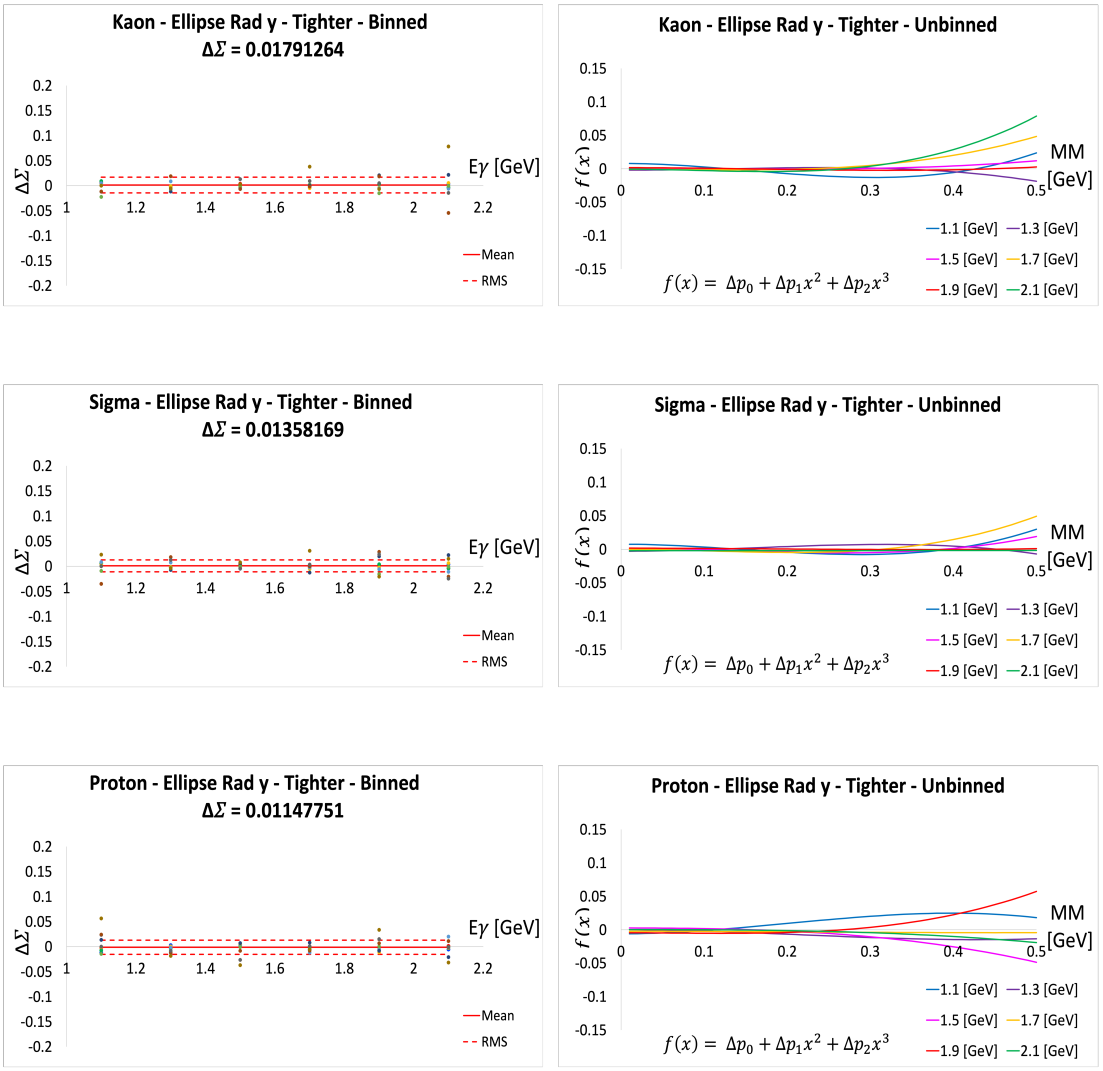

Figure 32: Systematic effects associated with the radius (in the y axis) of the elliptical cut.

4.6 Systematic effects of maximum likelihood

Previous works have investigated the systematic effects of the maximum likelihood technique [38][39][40]. All studies indicate the associated systematics are negligible.

5 Results

The overall objective of this analysis was to study the hyperon-nucleon interaction, by determining the beam spin asymmetry of the particles involved in the $\gamma d \to K^+\Sigma^-(p)$ reaction. As discussed in Sec. 3.7, the beam spin asymmetry Σ of a particle is diluted after any interaction or scattering event. The beam spin asymmetry was determined as a function of the missing momentum of the spectator proton for the K^+, Σ^- and the spectator proton. Producing results for all three particles allows a comparison between the extent of secondary scattering events for each particle. In particular, the results for the K^+ particle are compared to that of the Σ^- hyperon. Comparing the Σ of both particles showed which particle underwent a higher amount of interactions. The beam spin asymmetry of the proton gives information about the spectator processes which may have occurred during the reaction.

The results of both the binned and unbinned techniques are shown in Fig. 35. The results are very similar for both techniques, which improves confidence in the quality of the analysis. The results from the binned technique have incorporated uncertainty in Σ shown by the black error bars. The uncertainties in Σ from the unbinned technique were computed using the bootstrapping method described in Sec. 3.8 where the uncertainty is represented by the width of the plotted function (a larger width corresponds to a larger uncertainty in Σ).

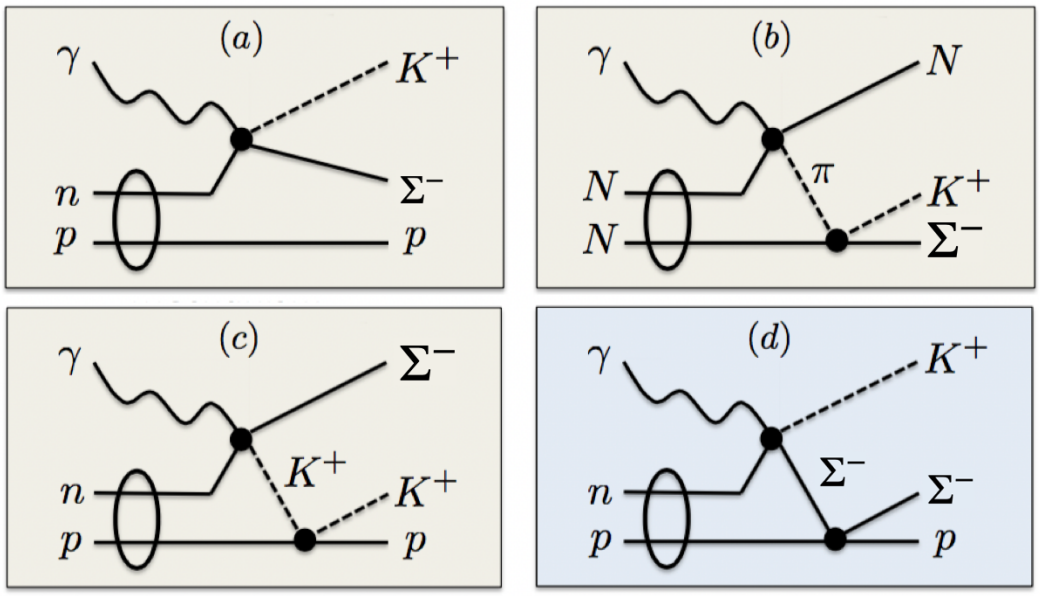

Figure 33: Four main mechanisms that contribute to the $\gamma d \to K^+\Sigma^-$ reaction: (a) quasi-free $K^+\Sigma^-$ photoproduction on the neutron. (b) pion mediated production. (c) K^+ rescattering off the spectator proton. (d) Σ^- rescattering off the spectator proton [37].

Fig. 33 shows the four main mechanisms that contribute to the $\gamma d \rightarrow K^+\Sigma^-$ reaction. Each one of these mechanisms would produce a different outcome to the beam spin asymmetry results for the K^+ and Σ^-. The quasi-free mechanism would lead to a high value of beam spin asymmetry that would be the same for both the K^+ and Σ^- particles (since neither undergoes any further interactions). The pion mediated mechanism would produce a beam spin asymmetry of 0 for both particles (given that the K^+ and Σ^- are not produced by the polarised photon) but produce a high beam spin asymmetry for the proton [42]. The K^+ rescattering mechanism would dilute the beam spin asymmetry more for the K^+ in comparison with the Σ^- baryon, with the opposite being true for the Σ^- rescattering mechanism. This analysis extracted the beam spin asymmetry of the K^+, Σ^- and the spectator proton. Matching these results with the expectations of each reaction mechanism reveals which of the reaction mechanisms was the most dominant.

The complete set of results can be seen on the following pages. One feature of the plots is the difference between the beam spin asymmetry values of the K^+ and Σ^- particles. The beam spin asymmetry is consistently diluted more for the Σ^- hyperon than for the K^+ at higher missing momenta. This indicates that at higher missing momenta the Σ^- rescattering mechanism is the most dominant.

The beam spin asymmetry of the spectator proton gives access to different information. In the reaction of interest, the spectator proton does not interact with the polarised photon beam. This, as well as the dynamics of this specific reaction, generates the expectation of the spectator proton having a beam spin asymmetry of 0. This expectation is in line with the final results. This further assures that the analysis completed was correct and that the cuts applied isolated the desired reaction of interest. It can also be observed that at times the beam spin asymmetry of the spectator proton deviates from its zero value. This information is also useful as it highlights the events in which the spectator underwent an interaction.

One of the main advantages of this particular method of analysis is the ability to extrapolate the beam spin asymmetry results to where missing momentum of the spectator proton is at 0. At missing momentum of 0 the deutron target can be viewed as a free neutron target. This is an especially important feature since free neutron targets do not exist in nature. The validity of the method used in this analysis could be tested by utilising the method on an analysis involving a proton target and comparing to free proton data.

The results from the two-fold binning are also shown below (the two-fold binning was only completed for the unbinned technique). Fig. 23 shows that the binned regions with more numerous available statistics were within the range $E_\gamma = 1.3 - 1.9$ GeV, for all values of $\cos\theta^{c.m.}_{K^+}$. A closer look at specific regions within this range (Fig. 37, 38, 39) shows the associated uncertainties to be much smaller than those of a low statistic region (for example $E_\gamma = 1.1 - 1.3$ GeV, $\cos\theta^{c.m.}_{K^+} < 0$). The following figure shows a comparison between the results of high statistic and low statistic regions:

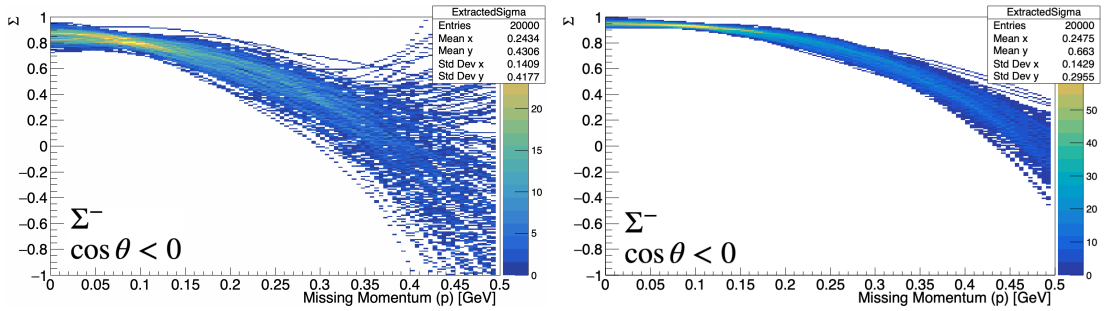

Figure 34: A comparison between the results of an example low statistic (left: $E_\gamma = 1.1 - 1.3$ GeV, $\cos\theta^{c.m.}_{K^+} < 0$) and high statistic (right: $E_\gamma = 1.7 - 1.9$ GeV, $\cos\theta^{c.m.}_{K^+} < 0$) regions. The low statistic region shows a greater uncertainty in Σ.

The objective of the two-fold binning method was to allow the isolation of kinematic regions in which the Σ^- scattering events were significantly more dominant than K^+ scattering events. These regions can be used in conjunction with theoretical approaches to tune the free parameters of the YN interaction and help to bring clarity to hyperon interactions [43]. The following is a list of kinematic regions within which the results showed a considerably more diluted beam spin asymmetry for Σ^- than the K^+:

- $E_\gamma = 1.3 - 1.5$ GeV, $\cos\theta^{c.m.}_{K^+} > 0$ (Fig. 37)
- $E_\gamma = 1.5 - 1.7$ GeV, $\cos\theta^{c.m.}_{K^+} < 0$ (Fig. 38)
- $E_\gamma = 1.7 - 1.9$ GeV, $\cos\theta^{c.m.}_{K^+} < 0$ (Fig. 39)

Another common feature of the result plots from these regions is the dilution of Σ occurring at high missing momenta, approximately at missing momenta above 0.3 GeV. This allows a further specification of the kinematic regions in which the Σ^- rescattering mechanism is dominant. Isolating kinematic regions through E_γ, $\cos\theta^{c.m.}_{K^+}$ and missing momenta can provide a basis for further theoretical work. Collaborative work with theorists is beginning with the objective of interpreting the results gathered by this analysis in an attempt to better constrain currently available hyperon-nucleon interaction models.

5.0.1 Σ results

The final results of the analysis are shown below. The results using the binned maximum likelihood method are shown in the left panels. The right panels show the results using the unbinned maximum likelihood method.

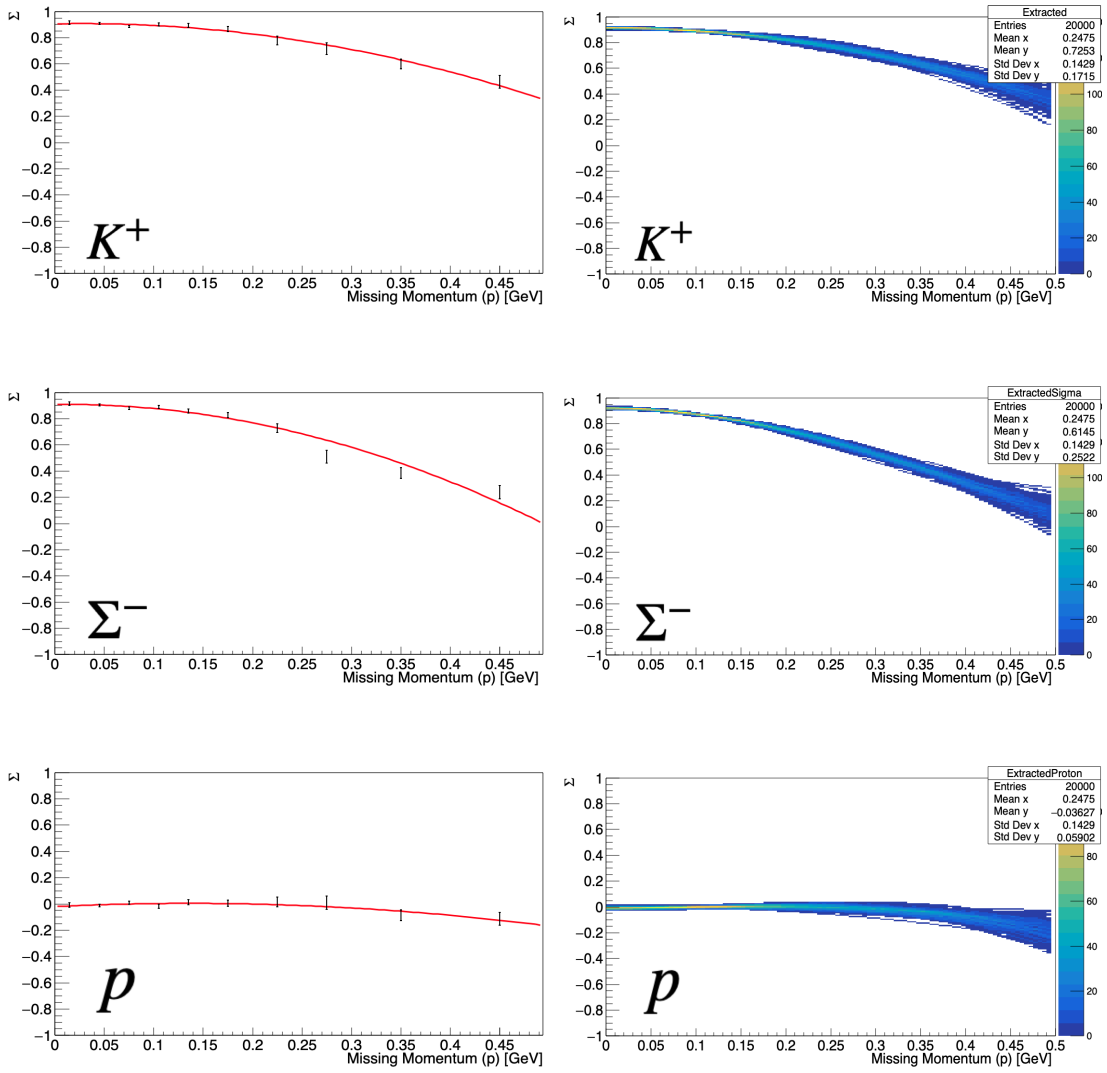

Figure 35

5.0.2 Two-fold binning results

It should be noted that the events were binned in E_γ even though the probability of the Σ^- rescattering is dependant only on its relative momentum. The quasi-free photoproduction and pion mediated production mechanisms (shown in Fig. 33) would produce different results for different values of E_γ, therefore binning in E_γ still had importance.

$E_\gamma = 1.1 - 1.3$ GeV

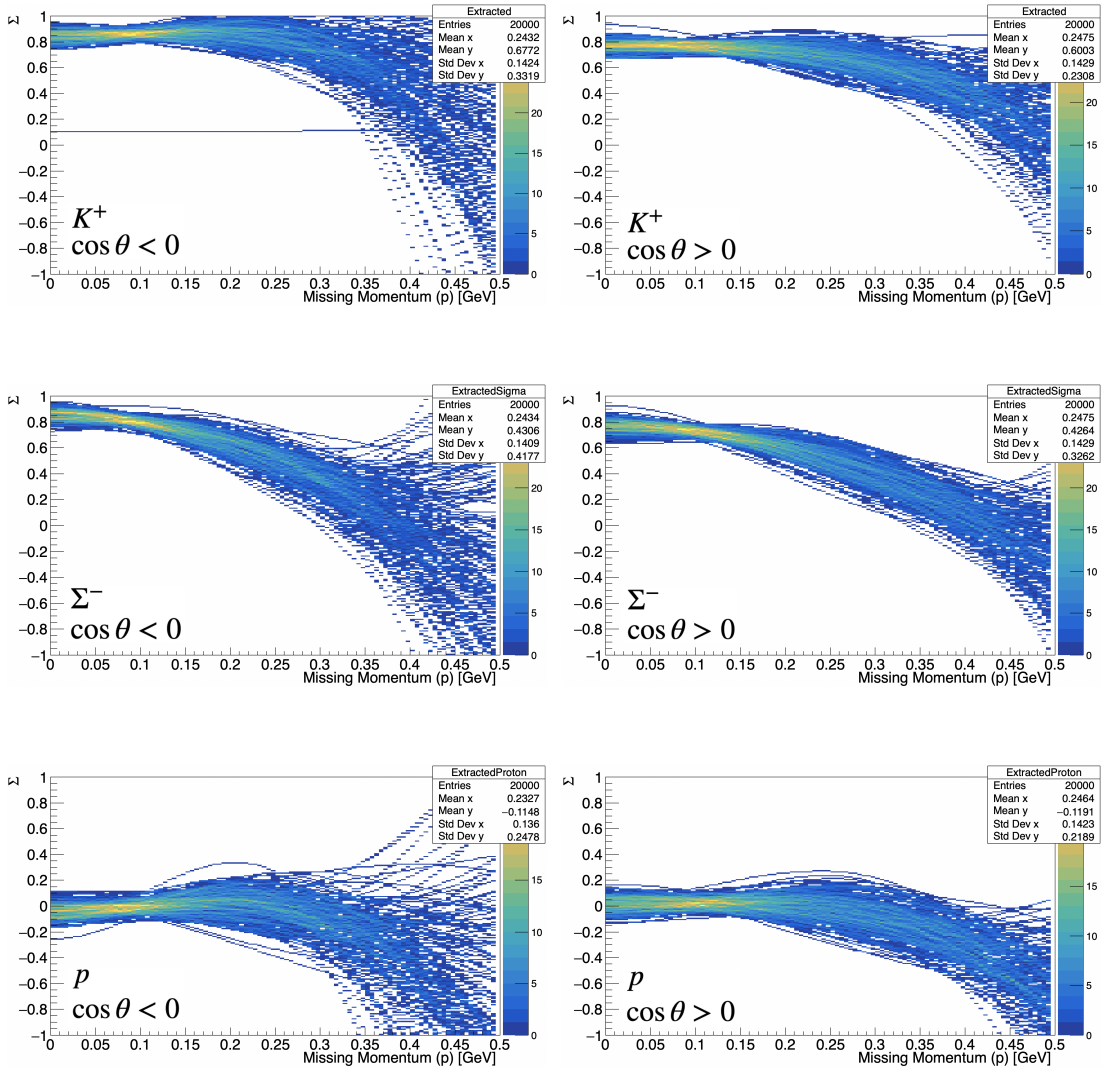

Figure 36

$E_\gamma = 1.3 - 1.5$ GeV

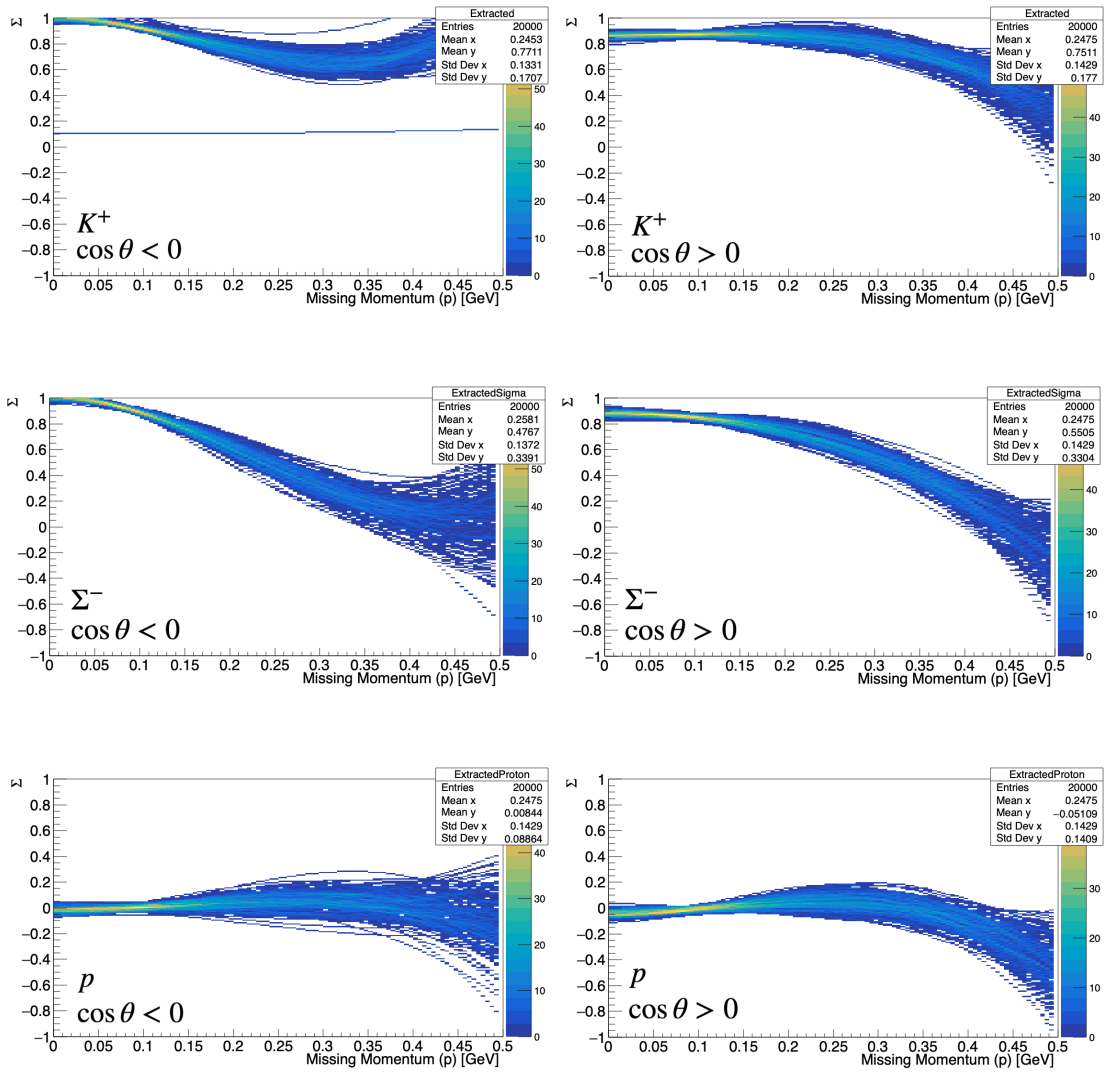

Figure 37

$E_\gamma = 1.5 - 1.7$ GeV

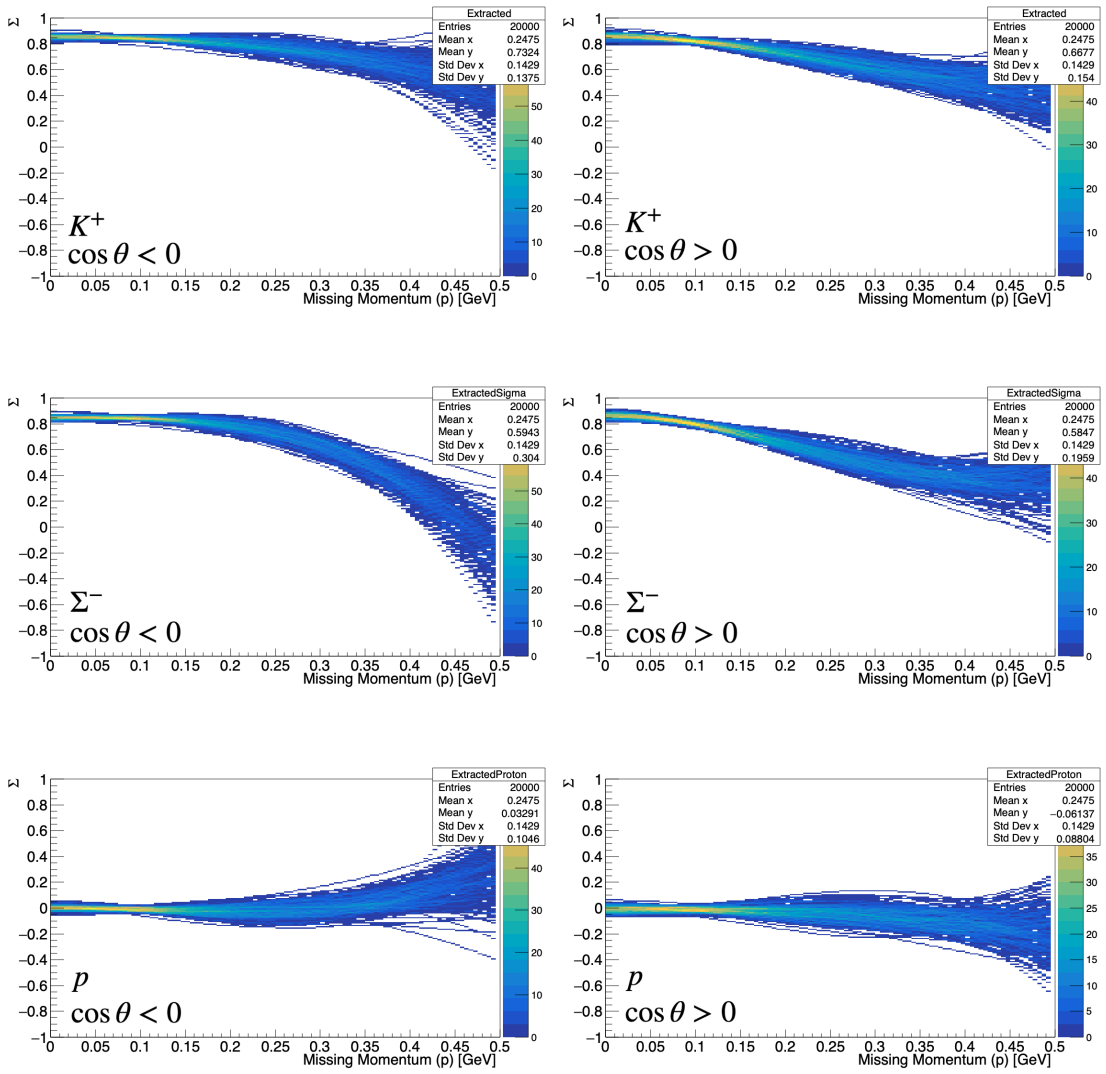

Figure 38

$E_\gamma = 1.7 - 1.9$ GeV

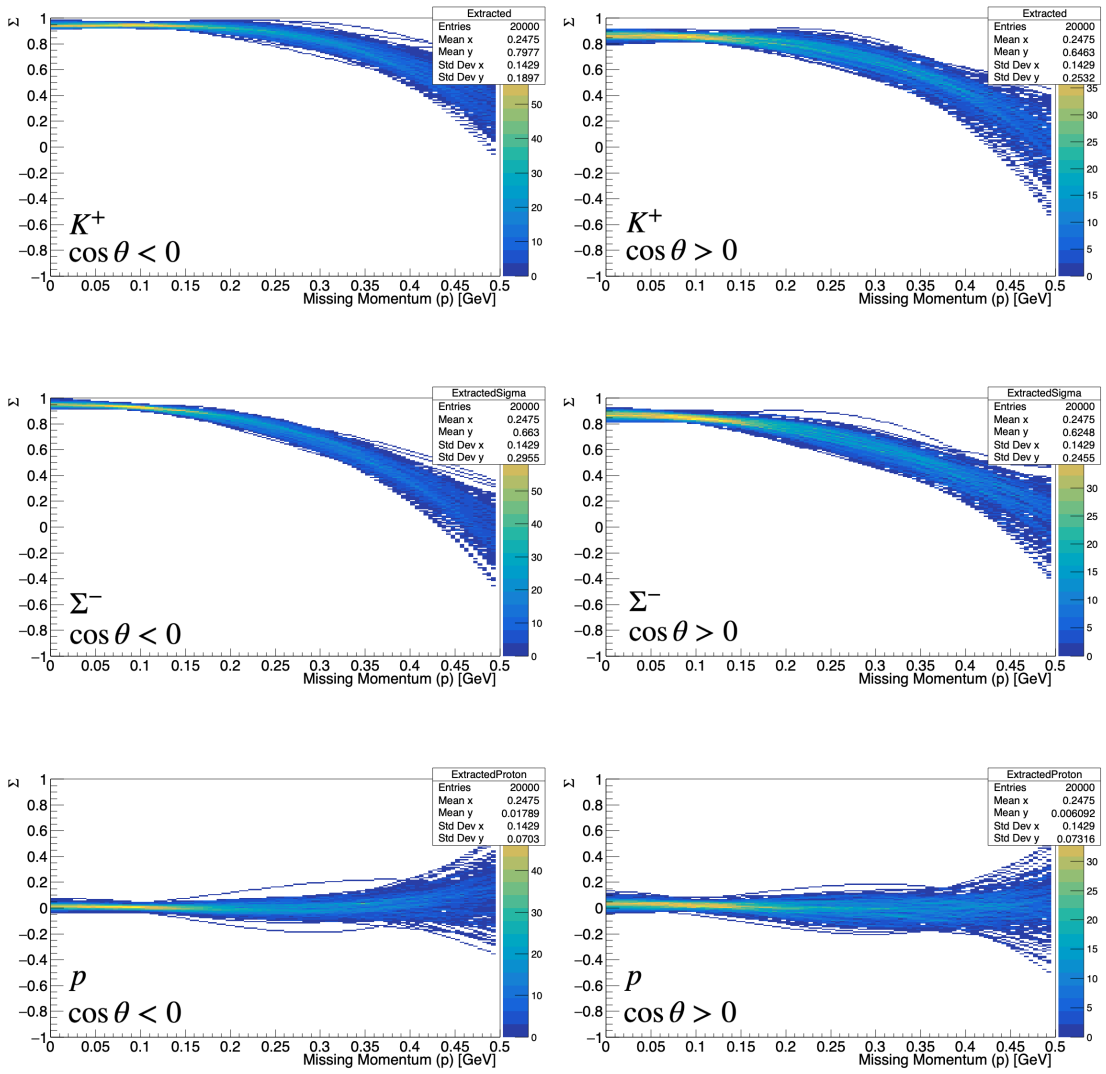

Figure 39

$E_\gamma = 1.9 - 2.1$ GeV

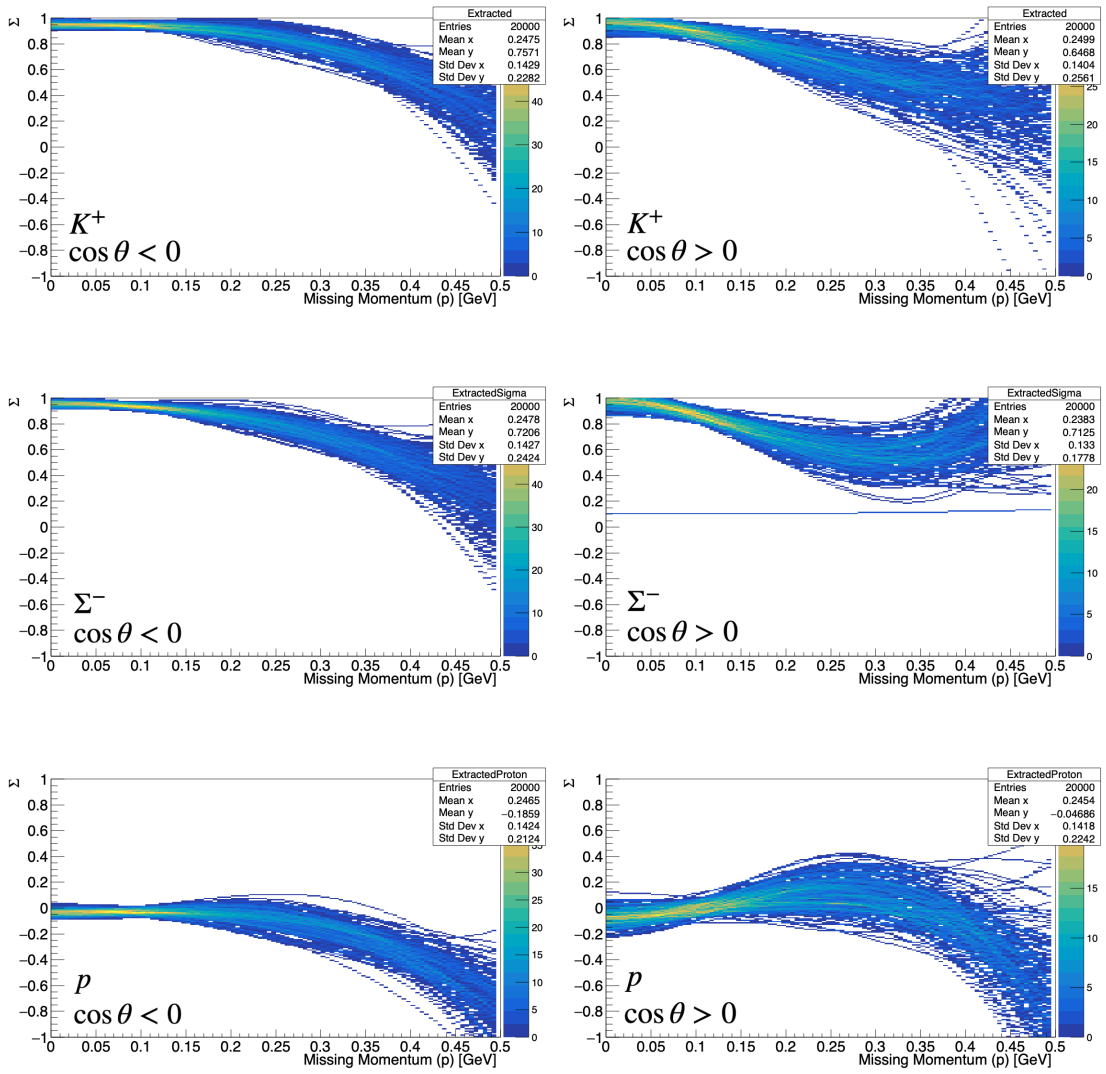

Figure 40

$E_\gamma = 2.1 - 2.3$ GeV

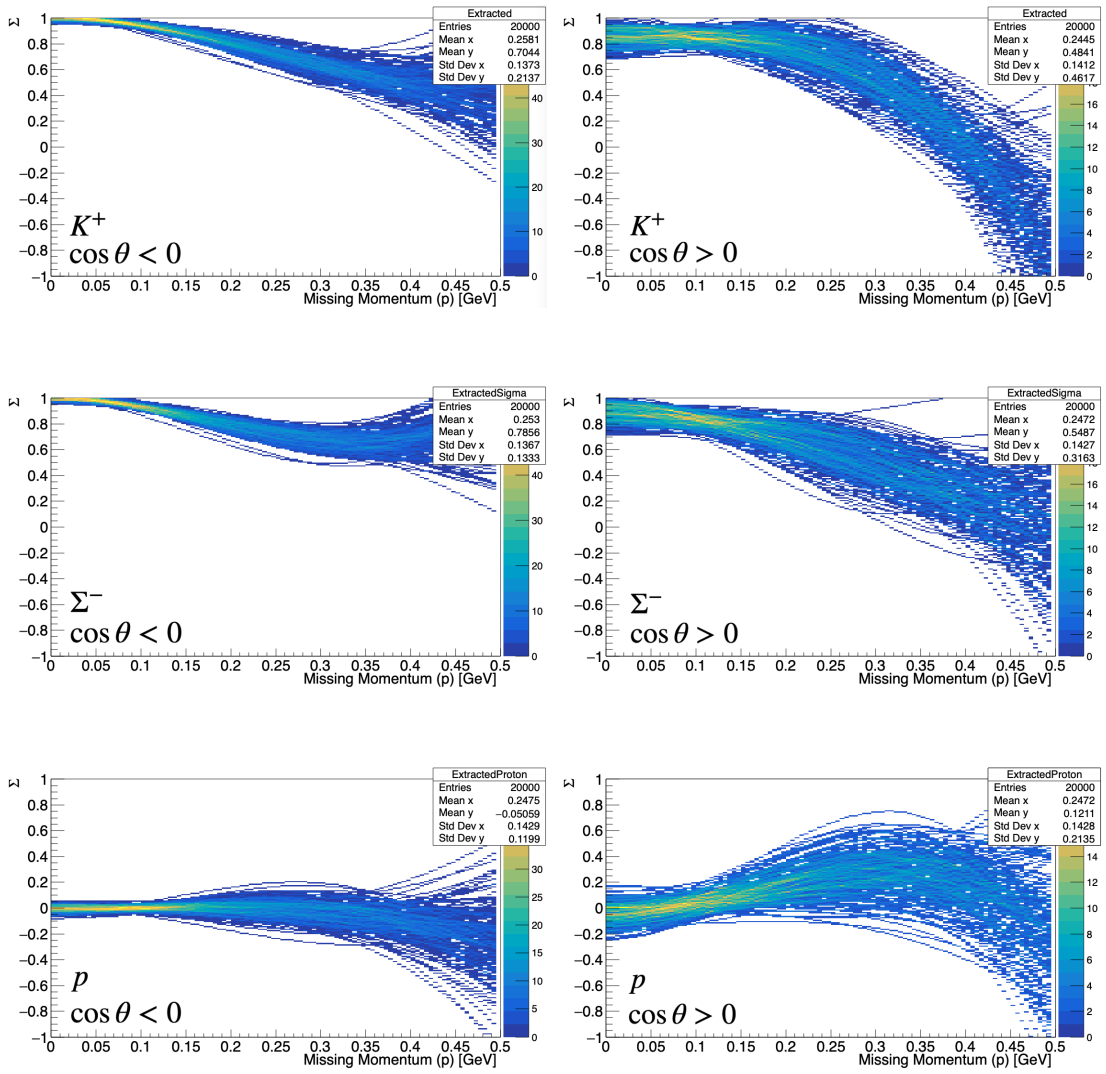

Figure 41

6 Summary

This work has presented the procedure and results of an analysis carried out on data collected using the CLAS detector housed at the Thomas Jefferson National Accelerator Facility.

The hyperon-nucleon (YN) interaction is not currently very well defined. In comparison with the nucleon-nucleon (NN) interaction, the available data for the YN interaction is sparse. Additionally, the data for the YN interaction have much bigger associated uncertainties. A better understanding of the YN interaction is crucial to a better understanding of the strong nuclear interaction.

Hyperons are believed to be present and stable within neutron stars. The hyperon puzzle is the name given to the discrepancy between current models of neutron stars made up of hyperons and previous observational evidence. This problem can be solved by including hyperon interactions, however, more must first be done to understand hyperon-nucleon, hyperon-hyperon and hyperon three-body interactions.

This analysis extracted the beam spin asymmetry (Σ) for the particles involved in the $\gamma d \rightarrow K^+\Sigma^-$ reaction. This was done using the maximum likelihood method. The results of the analysis point towards the Σ^- rescattering mechanism being the most dominant in the reaction of interest. The analysis also isolated kinematic regions within which the Σ^- interactions are especially dominant.

The results of this work provide the basis for future theoretical work that can be a step towards a more complete model of hyperon-nucleon interactions. This theoretical work is beginning through a collaboration with theorists with the aim of better constraining available YN models.

References

[1] J. J. Thomson. XL. cathode rays. *The London, Edinburgh, and Dublin Philosophical Magazine and Journal of Science*, 44(269):293–316, 1897.

[2] J. J. Thomson. XXIV. on the structure of the atom: An investigation of the stability and periods of oscillation of a number of corpuscles arranged at equal intervals around the circumference of a circle; with application of the results to the theory of atomic structure. *The London, Edinburgh, and Dublin Philosophical Magazine and Journal of Science*, 7(39):237–265, 1904.

[3] E. Rutherford. LXXIX. the scattering of α and β particles by matter and the structure of the atom. *The London, Edinburgh, and Dublin Philosophical Magazine and Journal of Science*, 21(125):669–688, 1911.

[4] N. Bohr. On the constitution of atoms and molecules. *Philos. Mag*, 26, 1913.

[5] I. Joliot-Curie and F. Joliot-Curie. *Émission de protons de grande vitesse par les substances hydrogénées sous l'influence des rayons [lambda] tres pénétrants*. Gauthier-Villars, 1932.

[6] J. Chadwick. Possible existence of a neutron [Letters to the Editor]. *Nature*, 129:312, 02 1932.

[7] J. Bromberg. The impact of the neutron: Bohr and Heisenberg. *Historical Studies in the Physical Sciences*, 3:307–341, 01 1971.

[8] Eugene Wigner – Facts. nobelprize.org. Nobel prize outreach AB 2021.

[9] W. Heisenberg. Über den bau der atomkerne. i. *Zeitschrift für Physik*, 77(1):1–11, 1932.

[10] H. Yukawa. On the interaction of elementary particles. *Progress of Theoretical Physics Supplement*, 17:1–10, 1935.

[11] C. M. G. Lattes, H. Muirhead, G. P. S. Occhialini, and C. F. Powell. Processes involving charged mesons. *Nature*, 159:694–696, 05 1947.

[12] G. D. Rochester and C. C. Butler. Evidence for the existence of new unstable elementary particles. *Nature*, 160:855–857, 12 1947.

[13] M. Gell-Mann. A schematic model of baryons and mesons. *Physics Letters*, 8:214–215, 01 1964.

[14] O. W. Greenberg. Spin and unitary-spin independence in a paraquark model of baryons and mesons. *Physical Review Letters*, 13(20):598, 1964.

[15] V. D. Hopper and S. Biswas. Evidence concerning the existence of the new unstable elementary neutral particle. *Physical Review*, 80(6):1099, 1950.

[16] P. A. Zyla et al. Review of particle physics. *Progress of Theoretical and Experimental Physics*, 2020(8), 08 2020. 083C01.

[17] F Sammarruca and Randy Millerson. The radius of the canonical-mass neutron star and chiral effective field theory. *Journal of Physics G: Nuclear and Particle Physics*, 46(2):024001, 2019.

[18] Jason W. T. Hessels, Scott M. Ransom, Ingrid H. Stairs, Paulo C. C. Freire, Victoria M. Kaspi, and Fernando Camilo. A radio pulsar spinning at 716 hz. *Science*, 311(5769):1901–1904, Mar 2006.

[19] W. Baade and F. Zwicky. Remarks on super-novae and cosmic rays [Letters to the Editor]. *Phys. Rev.*, 46:76–77, 1934.

[20] V. A. Ambartsumyan and G. S. Saakyan. The degenerate superdense gas of elementary particles. *Soviet Astronomy AJ*, 4:187–354, 1960.

[21] Proceedings of the 12th International Conference on Hypernuclear and Strange Particle Physics. *The hyperon puzzle in neutron stars*, 07 2017.

[22] D. Chatterjee and I. Vidana. Do hyperons exist in the interior of neutron stars? *The European Physical Journal A*, 52(2):1–18, 2016.

[23] F. Crawford et al. A survey of 56 midlatitude EGRET error boxes for radio pulsars. *The Astrophysical Journal*, 652:1499–1507, 12 2006.

[24] R. S. Lynch et al. The Green Bank Telescope 350 mhz drift-scan survey ii: Data analysis and the timing of 10 new pulsars, including a relativistic binary. *The Astrophysical Journal*, 763:81, 01 2013.

[25] B. A. Mecking et al. The CEBAF large acceptance spectrometer (CLAS). *Nuclear Instruments and Methods in Physics Research Section A: Accelerators, Spectrometers, Detectors and Associated Equipment*, 503(3):513–553, 2003.

[26] P Nadel-Turonski, BL Berman, Y Ilieva, A Tkabladze, and DG Ireland. Kaon production on the deuteron using polarized photons. *Jefferson Lab Experiment E06-103*, 2006.

[27] M. Dugger and B.G. Richie. Consistency corrections to the linear photon polarization for g8b data. *CLAS Note*, 2012:002.

[28] K. Livingston. Polarization from coherent bremsstrahlung enhancement. CLAS Note, 2011:20.

[29] D. Sokhan. Measurement of σ in π photoproduction on the neutron from the g13b dataset.

[30] Jefferson Lab experimental Hall B. https://www.jlab.org/hall-b/int-web/welcome.html.

[31] Sober D. I. et al. The bremsstrahlung tagged photon beam in Hall B at JLab. *Nuclear Instruments and Methods in Physics Research Section A: Accelerators, Spectrometers, Detectors and Associated Equipment*, 440(2):263–284, 2000.

[32] Y. G. Sharabian et al. A new highly segmented start counter for the CLAS detector. *Nuclear Instruments and Methods in Physics Research Section A: Accelerators, Spectrometers, Detectors and Associated Equipment*, 556(1):246–258, 2006.

[33] M. D. Mestayer et al. The CLAS drift chamber system. *Nuclear Instruments and Methods in Physics Research Section A: Accelerators, Spectrometers, Detectors and Associated Equipment*, 449(1-2):81–111, 2000.

[34] E. S. Smith et al. The time-of-flight system for CLAS. *Nuclear Instruments and Methods in Physics Research Section A: Accelerators, Spectrometers, Detectors and Associated Equipment*, 432(2-3):265–298, 1999.

[35] M. Amarian et al. The CLAS forward electromagnetic calorimeter. *Nuclear Instruments and Methods in Physics Research Section A: Accelerators, Spectrometers, Detectors and Associated Equipment*, 460(2-3):239–265, 2001.

[36] N. Zachariou and E. Munevar. Photon beam-spin asymmetry measurement from the $\gamma n \to k^+\sigma^-$ reaction from the g13 run period. *CLAS Analysis Note 2020-002*, 2020.

[37] N. Zachariou, D. Watts, and Y. Ilieva. Study of the hyperon-nucleon interaction via final-state interactions in exclusive reactions. *SciPost Physics Proceedings*, (3):026, 2020.

[38] N. Zachariou. Determination of polarisation observables in $\gamma d \to k^+\lambda n$ FSI. *CLAS Analysis Note 2016-103*, 2016.

[39] N. Zachariou. Determination of the double polarization observable for the reaction $\gamma n \to k^+\sigma^-$. *CLAS Analysis Note 2019-103*, 2019.

[40] N. Zachariou. G double-polarization observable for the reactions $\gamma p \to \pi^+ n$ and $\gamma p \to \pi^0 p$ from g9 (frost) data. *CLAS Analysis Note 2019-107*, 2019.

[41] Bradley Efron and Robert Tibshirani. The bootstrap method for assessing statistical accuracy. *Behaviormetrika*, 12(17):1–35, 1985.

[42] C. A. Paterson et al. Photoproduction of λ and σ^0 hyperons using linearly polarized photons. *Physical Review C*, 93(6):065201, 2016.

[43] K. Miyagawa, T. Mart, C. Bennhold, and W. Glöckle. Polarization observables in exclusive kaon photoproduction on the deuteron. *Physical Review C*, 74(3):034002, 2006.